The final version is available on https://doi.org/10.1016/j.jcp.2019.03.034.

Multi-particle model of coarse-grained scalar dissipation rate with volumetric tensor in turbulence

Shusei Tanaka[a], Tomoaki Watanabe[a,1,*], Koji Nagata[a]

[a] *Department of Aerospace Engineering, Nagoya University, Nagoya 464-8603, Japan*

Abstract

A multi-particle model is proposed for a coarse-grained scalar dissipation rate, where a coarse-grained quantity is defined with an ensemble average of spatially-distributed fluid particles within a finite volume. The model computes the coarse-grained scalar dissipation rate from coarse-grained scalar gradient with a subgrid scale model of a scalar dissipation rate, which requires length-scale estimation for particle distribution. A volumetric tensor that characterizes the particle distribution is used in the model for computing the length scale and coarse-grained scalar and velocity gradients from particles. The model is examined in a priori and posteriori tests. A priori test with direct numerical simulation database of turbulent planar jets shows that the present model works well for a wide range of length scale of particle distribution when the number of particles N_M is about 10-16. The model with $N_M \lesssim 10$ overestimates the coarse-grained scalar dissipation rate, while $N_M \gtrsim 16$ causes stronger dependence of the model on the length scale of particle distribution. The proposed model is tested in hybrid large-eddy-simulation/Lagrangian-particle-simulation (LES/LPS) of planar jets, where

---

[*] Corresponding author (+81-052-789-3279)
Email address: `watanabe.tomoaki@c.nagoya-u.jp` (Tomoaki Watanabe)

Preprint submitted to Journal of Computational Physics *August 9, 2022*

the coarse-grained scalar dissipation rate appears as an unknown variable in a mixing volume model that computes a molecular diffusion term based on a multi-particle interaction. LES/LPS and DNS yield a similar profile of root-mean-squared scalar fluctuation, which strongly depends on the scalar dissipation rate. Comparison of the mean scalar dissipation rate between the model and the DNS shows that the present model applied to the LES/LPS well predicts the coarse-grained scalar dissipation rate at various jet Reynolds number.

Keywords: Lagrangian simulation, scalar dissipation rate, turbulent mixing, Large eddy simulation

1. Introduction

Turbulent mixing plays an important role in chemical processes, where turbulence promotes mixing and transport of chemical substances, energy, and momentum. Design of chemical reactors is strongly influenced by nature of turbulent mixing.[1,2] Numerical simulations are widely used to study turbulent mixing of chemically reacting flows. Large eddy simulation (LES), which resolves a large-scale field, is attractive for simulating reacting flows at a moderate computational cost. LES relies on models for unresolved small scales, which are called a subgrid scale (SGS) model. Turbulence has strong influences on chemical reaction rate even for a simple reaction.[3,4,5,6,7] Model parameters in SGS models for chemical reaction rates can depend on problems.[8] Therefore, development of SGS models for turbulent reacting flows[9,8] is quite difficult, and such models are often practically restricted to specific chemical reactions and flow conditions.

LES is often combined with different methods that simulate reactive scalars to avoid modeling of SGS effects on chemical source terms. Such examples are conditional moment closure[10] and filtered density function method.[11,12] A Lagrangian approach, where reactive scalars are simulated with a large number of notional fluid particles, is particularly useful since chemical source terms appear in a closed form.[13,14,15,16] A similar hybrid Eulerian/Lagrangian approach is also used in simulations of turbulent dispersed flows.[17,18,19] The Lagrangian simulation of reacting flows requires a model for molecular diffusion. This model is often called a mixing model. A large number of the mixing models have been developed in previous studies.[20,21,22,23,24,25] Most mixing models include a model parameter called a mixing timescale τ_M that controls dissipation rate of scalar fluctuations. It should be noted that the mixing model developed in the context of numerical simulations with Reynolds-Averaged-Navier–Stokes (RANS) equations should not be used for LES in the same form. Even if the scheme of the mixing model is similar between LES and RANS, there is difference in the definition of τ_M. One of the most common mixing models in RANS-type simulations is the interaction exchange with mean (IEM) model, which approximates the molecular diffusion term with a relaxation process of scalar to a Reynolds-averaged value. τ_M in the IEM model is obtained from the governing equation for scalar variance, where τ_M is also defined with Reynolds-averaged quantities.[23] An extension of the classical IEM model to LES was given for both compressible and incompressible flows in our previous papers as a mixing volume model (MVM),[25,26,27] which uses a relaxation process to a low-pass filtered value computed with a spatial average within a finite volume. Instead of scalar variance, the transport equation for SGS scalar variance yields an expression of τ_M in the MVM, which includes a coarse-grained scalar dissipation rate as an unknown variable. A similar extension of the classical Curl's model[20] based to LES was also given as the two-particle interaction scheme of the MVM.[25] It was also shown that the multi-particle interaction scheme of the MVM predicts molecular diffusion better than the two-particle interaction scheme[26]. These studies have shown that accurate estimation of the coarse-grained scalar dissipation rate is crucial in hybrid LES/Lagrangian-simulation with a mixing model.

Models for the coarse-grained scalar dissipation rate (or a SGS scalar dissipation rate) have been developed for grid-based simulations.[28,29,30] These models cannot directly be applied to estimate the coarse-grained scalar dissipation rate from particles. The model can compute the coarse-grained scalar dissipation rate on computational grids, and it might be interpolated onto the particle position.[26] However, this approach cannot take into account length-scale dependence of the coarse-grained scalar dissipation rate, since the length scales that characterize particle distribution and computational grids are generally different. In this sense, the coarse-grained scalar dissipation rate estimated on computational grids of LES is not adequate for Lagrangian simulations.

A more desirable method is modeling the coarse-grained scalar dissipation rate directly from particles. However, this has hardly been discussed in existing literatures of mixing models. In the present study, a multi-particle model is presented for the coarse-grained scalar dissipation rate. This model is developed based on a coarse-grained gradient estimation method from randomly distributed points[31] and a SGS model for the scalar dissipation rate.[29] Here, a coarse-grained scalar gradient is estimated from 4 particles or more based on scalar values at the particle positions, where relative positions of the particles are described by a 3×3 matrix called a volumetric tensor.[32,33,34] It has been shown that the volumetric tensor is useful for computing coarse-grained scalar and velocity gradients from randomly distributed points in turbulence.[31] The volumetric tensor plays an important role in the present model since it also quantifies the length scale of particle distribution. In this study, a priori test is performed for the proposed multi-particle model of the coarse-grained scalar dissipation rate with direct numerical simulation (DNS) database of turbulent planar jets.[26] The model is easily combined with the multi-particle MVM[26] in the Lagrangian simulations. A posteriori test is also performed by implementing the model in LES/Lagrangian-particle-simulation (LES/LPS) with the mixing volume model. The results of the LES/LPS of the turbulent planar jets are compared with the DNS database.

The paper is organized as follows. Section 2 describes the methodology of LES/LPS of passive scalar mixing with the MVM, where the coarse-grained scalar dissipation rate appears as an unknown variable. The main contribution of this paper is in Sec. 3, which presents the model of the coarse-grained scalar dissipation rate for Lagrangian computational particles. A priori and posteriori tests are reported in Secs. 4 and 5, respectively. Finally, the conclusion is given in Sec. 6.

2. Large eddy simulation combined with Lagrangian particle simulation of passive scalar mixing

2.1. Governing equations

The present study considers passive scalar mixing in an incompressible Newtonian fluid, where passive scalar does not affect the flow field (such as concentration of dissolved substance in dilute solution). The problem can be described by the Navier–Stokes equations and the scalar transport equation that describe the evolution of instantaneous velocity and passive scalar fields:

$$\begin{aligned}
\frac{\partial u_j}{\partial x_j} &= 0, &(1)\\
\frac{\partial u_i}{\partial t} + \frac{\partial u_i u_j}{\partial x_j} &= -\frac{\partial p}{\partial x_i} + \nu \frac{\partial^2 u_i}{\partial x_j \partial x_j}, &(2)\\
\frac{\partial \phi}{\partial t} + \frac{\partial u_j \phi}{\partial x_j} &= D \frac{\partial^2 \phi}{\partial x_j \partial x_j}, &(3)
\end{aligned}$$

where $i, j = 1, 2$, and 3 denote indices that represent the directions x, y, and z, respectively, t is time, u_i is velocity in the i direction, p is pressure divided by constant fluid density, ϕ is passive scalar, ν is kinematic viscosity, and D is diffusivity coefficient for ϕ. The summation is taken for the repeated subscript index. This rule is also applied throughout the paper.

We consider the hybrid Eulerian/Lagrangian simulation, where Eqs. (1) and (2) are solved with LES in a Eulerian setting while Eq. (3) is solved in a Lagrangian setting. A resolved (grid-scale) component of f in the LES is denoted by $\tilde{f}$. The governing equations for the LES are the filtered Navier-Stokes equations:

$$\frac{\partial \tilde{u}_j}{\partial x_j} = 0, \qquad (4)$$

$$\frac{\partial \tilde{u}_i}{\partial t} + \frac{\partial \tilde{u}_i \tilde{u}_j}{\partial x_j} = -\frac{\partial \tilde{p}}{\partial x_i} + \nu \frac{\partial^2 \tilde{u}_i}{\partial x_j \partial x_j} + R_i, \tag{5}$$

where R_i is the term related to unresolved scales. The Lagrangian simulation considers the scalar field represented by a large number of notional particles to which passive scalar values are assigned.[13] This approach is particularly useful when the scalars are mass fractions of chemicals since the chemical reaction term appears in a closed form unlike the LES of reactive scalar transport equations in the Eulerian setting. The computational particles considered in this study are fluid particles (i.e. Lagrangian objects), which can be defined as a point that moves with the local fluid velocity.[35]

The equation for ϕ along the particle path is solved in the simulation. Each particle is characterized by its position $\mathbf{x}^{(n)}$ in physical space and scalar value $\phi^{(n)}$ at $\mathbf{x}^{(n)}$, where superscript (n) represents nth particle ($n = 1, ..., N_p$). The hybrid LES/LPS solves the following modeled equations[26]:

$$\frac{d\mathbf{x}^{(n)}}{dt} = \tilde{\mathbf{u}}^{(n)}(t) = \tilde{\mathbf{u}}[\mathbf{x}^{(n)}(t); t], \tag{6}$$

$$\frac{d\phi^{(n)}}{dt} = \left[D\nabla^2\phi\right]^{(n)}_{\mathrm{mix}}, \tag{7}$$

where $\tilde{\mathbf{u}}$ is obtained from the LES and the subscript mix denotes a quantity computed by a mixing model. If the passive scalar is a mass fraction of chemicals, Eq. (7) is solved for mass fraction of each chemical, where a chemical source term is added in the right-hand side. This term is usually given as a function of scalar values assigned to the particles.[23] In most turbulent flows, the direct influences of the SGS velocity fluctuations on profiles of mean scalar and scalar variance appear as their turbulent transports and the production of scalar variance. However, these terms are dominated by large scales, which are well resolved by the filtered velocity field.[36] Therefore, at least, until the second-order statistics, the approximation with $\tilde{\mathbf{u}}$ in Eq. (6) is expected to be valid in turbulent flows. Another influence of the SGS velocity fluctuations appears in particle positions in the SGS. The relative position of particles is important in the model for molecular diffusion discussed below. In most applications of the LES/LPS, the characteristic distance among particles is greater than the grid size of the LES. In this case, the relative position of particles is dominated by the grid-scale velocity, and small changes in the particle positions in the SGS hardly affect the relative position of particles.

2.2. Mixing volume model

The mixing volume model (MVM)[26] is developed for Eq. (7) based on the interaction among spatially-distributed Lagrangian particles. The MVM is an extension of the classical IEM model. Each particle has a scalar value $\phi^{(n)}$ $(n = 1, ..., N_P)$ in the LPS. In the MVM, the effect of molecular diffusion for one particle is modeled by the interaction among $N_M \geq 2$ mixing particles, by which $\phi^{(n)}$ of the mixing particles is changed. In this paper, the particles used for this interaction are called mixing particles, while a virtual volume that contains N_M mixing particles is called a mixing volume. The shape and size of the mixing volume is arbitrary although which particles the volume contains is important in the model. In practice, for particle n, $N_M - 1$ mixing particles are selected in the descending order according to the distance from particle n. This method for selecting particles ensures that the mixing is localized in physical space. The MVM is based on a relaxation process to average within a mixing volume. Hereafter, V_M^n denotes the mixing volume set up for particle n. The average within the mixing volume V_M^n is expressed by an ensemble average of the mixing particles in V_M^n:

$$\langle f|V_M^n\rangle = \frac{1}{N_M}\sum_{\alpha=1}^{N_M} f^{(\alpha)}, \tag{8}$$

where $\alpha = 1, ..., N_M$ is used as an integer that represents N_M mixing particles in V_M^n. A fluctuation from $\langle f|V_M^n\rangle$ is denoted by $f''^{(\alpha)} = f^{(\alpha)} - \langle f|V_M^n\rangle$. The MVM for the mixing volume of particle n changes the scalar values of the mixing particles by the following equation

$$[D\nabla^2\phi]_{\mathrm{mix}}^{(\alpha)} = \frac{1}{\tau_M}\left(\langle\phi|V_M^n\rangle - \phi^{(\alpha)}\right) \quad \text{for } \alpha = 1, ..., N_M, \tag{9}$$

with the mixing timescale τ_M, which controls the scalar dissipation rate. The model, Eq. (9), changes the scalar value of the mixing particles, where the same value of $\langle\phi|V_M^n\rangle$ evaluated before the interaction is used for all mixing particles in V_M^n.

The average within the mixing volume V_M^n can be expressed with the kernel function G_n by

$$\langle f|V_M^n\rangle = \frac{\sum_{m=1}^{N_P} G_n(\mathbf{x}^{(m)})f^{(m)}}{\sum_{m=1}^{N_P} G_n(\mathbf{x}^{(m)})}, \tag{10}$$

$$G_n(\mathbf{x}^{(m)}) = \begin{cases} 1 & \text{If } \mathbf{x}^{(m)} \text{ is in mixing volume } V_M^n \\ 0 & \text{otherwise} \end{cases}. \tag{11}$$

The volume average with the kernel function G_n yields the low-pass filtered value with a box filter whose cutoff length is related to the size of the mixing volume. A variance in the mixing volume, $\langle f''^2|V_M^n\rangle = \langle f^2|V_M^n\rangle - \langle f|V_M^n\rangle^2$, is related to the fluctuation in small scales. The MVM, Eq. (9), results in decay of the scalar variance in the mixing volume. Therefore, the expression of τ_M is derived from the transport equation for the scalar variance within the mixing volume, $\langle \phi''^2 | V_M^n \rangle$,[25] where τ_M is given by

$$\tau_M = \frac{\langle \phi''^2 | V_M^n \rangle}{\langle \varepsilon_\phi | V_M^n \rangle}. \tag{12}$$

Here, $\varepsilon_\phi = D \nabla \phi \cdot \nabla \phi$ is the scalar dissipation rate. The mixing timescale τ_M is a key quantity in the model since it controls the decay rate of scalar variance. Most previous studies have modeled the mixing timescale with a flow timescale τ and a model parameter C as $\tau_M = C\tau$. The problem of the assumption $\tau_M = C\tau$ is in the method for choosing C, which can be different depending on flow types. C is usually treated as a constant even though it can depend on position and time.[37,15] Therefore, usage of the constant C is likely to result in inaccurate estimation of the local mixing timescale even though one can adjust C so that the averaged mixing timescale is optimized for each problem.

Although $\langle \phi''^2 | V_M^n \rangle$ in Eq. (12) can be computed from $\phi^{(n)}$ defined at the particle positions, the coarse-grained (or low-pass filtered) scalar dissipation rate $\langle \varepsilon_\phi | V_M^n \rangle$ needs to be modeled to close the equations that describe the particle evolution since the particle field, in most cases, does not have a high resolution enough to compute a fully-resolved scalar gradient $\nabla \phi$.

3. Multi-particle model for coarse-grained scalar dissipation rate

This section presents the multi-particle model for coarse-grained scalar dissipation rate defined as $\langle \varepsilon_\phi | V_M^n \rangle$. The model is developed based on the coarse-grained gradient estimation method with the volumetric tensor[31] and the SGS model for scalar dissipation rate, which was originally proposed for Eulerian simulations.[29]

3.1. Volumetric tensor and coarse-grained gradient

We assume that $N_M \geq 4$ mixing particles participate the mixing event with particle n. Since the MVM is described with the ensemble average of the mixing particles, the shape and size of V_M^n have no direct influences on the model while how to select the mixing particles is important. Once the mixing particles are selected, V_M^n can be considered as the volume that contains particle n and $N_M - 1$ mixing particles. The average within the mixing volume is computed simply as an ensemble average of N_M particles by Eq. (8). Then, the center position of the particles within V_M^n is given by $\langle \mathbf{x} | V_M^n \rangle$.

The position of particle α in relation to the center is

$$\mathbf{r}^{(\alpha)} = \mathbf{x}^{(\alpha)} - \langle \mathbf{x} | V_M^n \rangle. \tag{13}$$

We introduce the volumetric tensor[33] that characterizes the distribution of the particles within V_M^n. The volumetric tensor is a 3×3 matrix defined as

$$R_{ij} = \langle r_i r_j | V_M^n \rangle, \tag{14}$$

which has three real eigenvalues R_a^2, R_b^2, and R_c^2 ($R_a^2 \geq R_b^2 \geq R_c^2$), where the corresponding eigenvectors are $\mathbf{a}$, $\mathbf{b}$, and $\mathbf{c}$. The spatial distribution of the particles can be approximated by an ellipsoid shape whose major, middle, and minor semi axes are, respectively, given by R_a, R_b, and R_c with their directions of $\mathbf{a}$, $\mathbf{b}$, and $\mathbf{c}$. The ellipsoid shape can be evaluated by parameters called elongation $E = 1 - R_b/R_a$ and planarity $P = 1 - R_c/R_b$.[32] E and P have a value between 0 and 1 depending on the shape of the ellipsoid. When the ellipsoid is elongated in one direction, E is close to 1. On the other hand, the ellipsoid with a flat shape has $P \approx 1$. Both E and P have small values for a quasi-spherical shape.

The mean separation distance between the particle and the center $\langle \mathbf{x} | V_M^n \rangle$ is given by $\sqrt{R_a^2 + R_b^2 + R_c^2}$. Therefore, the characteristic length scale of the mixing volume can be estimated as

$$L_{VT} = 2\sqrt{R_a^2 + R_b^2 + R_c^2} = 2\sqrt{\mathrm{tr}(R_{ij})}. \tag{15}$$

L_{VT} also characterizes the cutoff length scale of the low-pass filter defined as an ensemble average of particles since this average is given by the volume average within V_M^n. Equation (15) gives a single length scale for the volume. If the volume is anisotropic ($E \gg 0$ and $P \gg 0$), the characteristic length scale of the mixing volume also depends on directions. As shown in the next section, the distribution of randomly distributed particles has small E and P when the number of particles is large.

It was shown that the volumetric tensor can be used for computing a coarse-grained gradient of flow variables given at randomly distributed computational points in turbulent flows.[31] This gradient estimation method is used with the particles within the mixing volume. A coarse-grained gradient of f, $\langle \partial f / \partial x_j | V_M^n \rangle$, can be estimated based on a linear approximation as[31]

$$\left\langle \frac{\partial f}{\partial x_j} \middle| V_M^n \right\rangle = \frac{1}{2N_M} \sum_{\alpha=1}^{N_M} \sum_{\beta=1}^{N_M} (f^{(\alpha)} - f^{(\beta)})(r_k^{(\alpha)} - r_k^{(\beta)}) R_{kj}^{-1}, \tag{16}$$

where R_{ij}^{-1} is the inverse of the volumetric tensor R_{ij}, the summation is taken for the repeated index k, and the integers α and β denote N_M particles within V_M^n. Although Eq. (16) can be used for $N_M \geq 4$ particles, $\langle \partial f / \partial x_j | V_M^n \rangle$ is poorly estimated by Eq. (16) in the case of $N_M \leq 6$, for which the spatial distribution of randomly distributed particles tends to be anisotropic.[31]

3.2. Coarse-grained scalar dissipation rate

The present multi-particle model computes the coarse-grained scalar dissipation rate $\langle \varepsilon_\phi | V_M^n \rangle$ with the coarse-grained gradient $\langle \partial\phi/\partial x_j | V_M^n \rangle$ and the quantities assigned to particles ($\mathbf{x}^{(n)}$, $\tilde{\mathbf{u}}^{(n)}$, and $\phi^{(n)}$). A SGS model for the filtered scalar dissipation rate proposed by Cook and Bushe[29] is applied to the particles within V_M^n, where $\langle \varepsilon_\phi | V_M^n \rangle$ is expressed by

$$\langle \varepsilon_\phi | V_M^n \rangle = C_{\varepsilon\phi} D \left\langle \frac{\partial\phi}{\partial x_j} \middle| V_M^n \right\rangle \left\langle \frac{\partial\phi}{\partial x_j} \middle| V_M^n \right\rangle , \tag{17}$$

where $C_{\varepsilon\phi}$ is a model parameter. Equation (17) is computed for Lagrangian particles while the original model by Cook and Bushe[29] was developed for estimating the filtered scalar dissipation rate on a computational grid of LES.

In the case that the particle distribution is too sparse to resolve scalar gradient, $C_{\varepsilon\phi}$ has a value much greater than 1. This situation is usually encountered in the simulation of turbulent flows at high Reynolds number because the length scale related to the scalar gradient becomes smaller with the Reynolds number. If the scalar gradient is fully resolved by the particles, $C_{\varepsilon\phi}$ is close to 1 because of $\langle \partial\phi/\partial x_j | V_M^n \rangle \approx \partial\phi/\partial x_j$ and $\langle \varepsilon_\phi | V_M^n \rangle \approx \varepsilon_\phi$.

The estimation of $C_{\varepsilon\phi}$ based on an energy spectrum for scalar fluctuation E_ϕ is also proposed in a Eulerian setting by Cook and Bushe,[29] and it is extended for the particles within the mixing volume in this study. Here, E_ϕ is used to estimate the scalar dissipation rate caused by all length scales or resolved scales by particles. The scalar dissipation rate is mostly contributed by small scales in turbulent flows. E_ϕ in small scales is less sensitive to flows than in large scales. Therefore, a model of E_ϕ studied in canonical isotropic turbulence is useful in estimation of the fraction of the scalar dissipation rate caused by the resolved scales. Although E_ϕ is not the same as the spectrum of ϕ simulated by particles, the model of E_ϕ is expected to give a good approximation of the spectral shape in small scales. Hereafter, E_ϕ given by a model spectrum in isotropic turbulence is considered. For the coarse-grained field in the mixing volume V_M^n, $C_{\varepsilon\phi}$ is estimated by

$$C_{\varepsilon\phi} = \frac{\int_0^\infty k^2 E_\phi(k) dk}{\int_0^\infty k^2 \hat{G}^2(k, L_{VT}) E_\phi(k) dk}, \tag{18}$$

where the numerator and denominator are, respectively, related to the scalar dissipation rate from all length scales, $\langle \varepsilon_\phi | V_M^n \rangle$, and from scales larger than L_{VT}, $D \langle \partial\phi/\partial x_j | V_M^n \rangle \langle \partial\phi/\partial x_j | V_M^n \rangle$, where L_{VT} is defined with the volumetric tensor as the characteristic length of the particle distribution in Eq. (15). The low-pass filter $\hat{G}(k, L_{VT})$ in wavenumber space corresponds to the volume average $\langle f | V_M^n \rangle$ with the cutoff length L_{VT}. The volume average with G_n defined by Eq. (11) works as a box filter in physical space. Therefore, the multi-particle model uses the spectral transfer function for the box filter[35] as $\hat{G}(k, L_{VT})$:

$$\hat{G}(k, L_{VT}) = \frac{\sin(k L_{VT}/2)}{k L_{VT}/2}. \tag{19}$$

Even though the box filter causes oscillations in the wavenumber space, this filter is used here because it is equivalent to ensemble average of particles used for computing the volumetric tensor. Cook and Bushe[29] used the following model spectrum in Eq. (18) for $Sc \approx 1$:

$$E_\phi(k) = A k^{-5/3} \mathrm{exp}\left[-1.73(k L_\phi)^{-4/3} - 2.25(k\eta_\phi)^{4/3}\right], \tag{20}$$

with the integral length scale L_ϕ and the smallest scale η_ϕ in the scalar field. The constant A, which appears both in the numerator and denominator in

Eq. (18), does not affect $C_{\varepsilon\phi}$. The length scales are estimated from the particles within the mixing volume by:

$$
\begin{aligned}
L_\phi &= 3\sqrt{\frac{k_r}{S_V^2}}, && (21)\\
\eta_\phi &= Sc^{-1/2}\eta_V, && (22)\\
\eta_V &= 1.5Re_l^{-3/4}L_\phi, && (23)\\
Re_l &= \frac{L_\phi\sqrt{k_r}}{\nu}, && (24)\\
k_r &= \langle \tilde{u}_j\tilde{u}_j|V_M^n\rangle - \langle \tilde{u}_j|V_M^n\rangle\langle \tilde{u}_j|V_M^n\rangle, && (25)\\
S_V^2 &= \frac{1}{4}\left(\left\langle\frac{\partial\tilde{u}_i}{\partial x_j}\middle|V_M^n\right\rangle+\left\langle\frac{\partial\tilde{u}_j}{\partial x_i}\middle|V_M^n\right\rangle\right)\left(\left\langle\frac{\partial\tilde{u}_i}{\partial x_j}\middle|V_M^n\right\rangle+\left\langle\frac{\partial\tilde{u}_j}{\partial x_i}\middle|V_M^n\right\rangle\right) && (26)
\end{aligned}
$$

Similar estimations of the length scales were used on a computational grid by Cook and Bushe,[29] where important difference in above equations from Cook and Bushe,[29] is that the length scales are estimated from the particles within the mixing volume. Here, the coarse-grained velocity gradient $\langle\partial\tilde{u}_i/\partial x_j|V_M^n\rangle$ in Eq. (26) is also computed from the particles within V_M^n with Eq. (16). k_r is the kinetic energy in the particle motion in relation to the mean motion of the particles, while S_V^2 is the product of the coarse-grained strain-rate tensor. Here, we assume that the grid size in LES is smaller than the size of the mixing volume. These parameters in the scalar spectrum are estimated by the characteristics of turbulence because scalar fluctuations are assumed to be produced by turbulent velocity fluctuations. It should be noted that the definition of the kinetic energy in the length scale estimation is different from Cook and Bushe[29]: they have used the kinetic energy of the filtered velocity, which contains the contribution of the mean flow of resolved scales. We found that the length scale estimation with k_r, Eq. (25), works better in a laminar region with a mean flow since the kinetic energy in the mean flow is not directly related to the length scales of turbulence.

The equations presented above enable us to compute the coarse-grained scalar dissipation rate from particles within a finite volume without any arbitrary constants. When the model is combined with the MVM, the coarse-grained scalar dissipation rate is computed for all mixing volumes considered in the simulation.

Schmidt-number dependence of the coarse-grained scalar dissipation rate is treated in the model by the scalar spectrum E_ϕ. In the case of $Sc \gg 1$, the scalar spectrum has a viscous-diffusive range with the smallest length scale defined as the Batchelor scale $\eta_B = \eta_K Sc^{-1/2}$. For $Sc \ll 1$, the scalar spectrum has an inertial-diffusive range with the smallest length scale, the Obukhov-Corrsin scale $\eta_{OC} = \eta_K Sc^{-3/4}$. The spectral shapes for the viscous-diffusive range and the inertial-diffusive range have been studied in previous studies.[38,39] For example, the scalar spectrum at large Schmidt number can be expressed with the form of $E_\phi(k) \sim k^{-1}\mathrm{exp}(-2k/k_B)$ for scales smaller than Kolmogorov scale η, where k_B is the wavenumber of the Batchelor scale $\eta_B = Sc^{-1/2}\eta$. The model spectra with the viscous-diffusive range or the inertial-diffusive range can be used for incorporating the Schmidt number dependence in the present model. The parameters in the model, such as the Batchelor scale and Obukhov-Corrsin scale, can be computed with the Schmidt number and the Kolmogorov scale computed with Eqs. (21-26).

4. A priori test of volumetric tensor model of scalar dissipation rate

4.1. DNS database of planar jet with passive scalar transfer

A priori test of the present model is performed with the DNS database of temporally-evolving planar jets with passive scalar transfer.[26] Temporally-evolving shear flows have been widely studied in DNS as a model of their spatially-evolving counterparts (e.g., jets,[40,41,42,43] mixing layers,[44,45,46] wakes,[47,48] and boundary layers[49,50,51,52]). These temporal simulations use periodic boundary conditions in a streamwise direction. The flow in temporal simulations develops with time instead of the streamwise direction. The planar jet in the temporal simulation is statistically one-dimensional and nonstationary, and it has different forms of averaged Navier-Stokes equations from spatially-evolving planar jets because the statistics in spatially-evolving planar jets are dependent on streamwise and cross-streamwise positions but independent of time. This results in the zero-mean cross-streamwise velocity in the temporal planar jet although the spatial one has mean inward velocity outside the jet. However, cross-streamwise profiles of root-mean-squared (rms) velocity fluctuations in the temporal planar jet are also consistent with those in spatially-evolving planar jets.[40,41] Analysis of the mean momentum equations in turbulent boundary layers also showed that the dominant term in the mean momentum equation is the same for both temporal and spatial simulations in turbulent boundary layers.[50] This is likely to be true in turbulent planar jets because both temporal and spatial planar jets have similar cross-streamwise profiles of mean streamwise velocity and Reynolds stress,[40,41] which appear in the dominant terms of the mean momentum equations.

One of the advantages of temporal simulations is a shorter streamwise computational domain than in spatial ones. This enables us to increase the Reynolds number in temporal simulations at a given computational resource. It is important to investigate the relation between the present model and length scales of turbulence, some of which are strongly dependent on the Reynolds number. The temporal planar jet is chosen as a test problem since a higher Reynolds number can be achieved than in the spatial jet. In contrast, one of the disadvantages is lack of convergence of statistics obtained in the temporal simulations.[50] This is because statistics are computed with a spatial average on homogeneous planes.

The DNS of temporally-evolving planar jets[40,41,43] uses a computational domain with periodic boundary conditions in the streamwise (x) and spanwise (z) directions, while the jet spreads with time in y direction. The lateral position of $y = 0$ is on the jet centerline. The components of velocity vector in x, y, and z directions are denoted by u, v, and w, respectively. At a given time step, the statistics are computed as a function of y by taking average in the x and z directions, where the average of a variable f is denoted by an overbar $\overline{f}$ and a fluctuation from the average is denoted by $f' = f - \overline{f}$. The flow is initialized with the mean velocity profile given by

$$\overline{u} = \frac{1}{2}U_J + \frac{1}{2}U_J \tanh\left(\frac{H - 2|y|}{4\theta_J}\right), \overline{v} = \overline{w} = 0, \tag{27}$$

where H is the initial jet width, $\theta_J = 0.015H$, and U_J is the jet velocity. The initial velocity profile is obtained by superimposing velocity fluctuations on the mean velocity, where the velocity fluctuations are generated with a

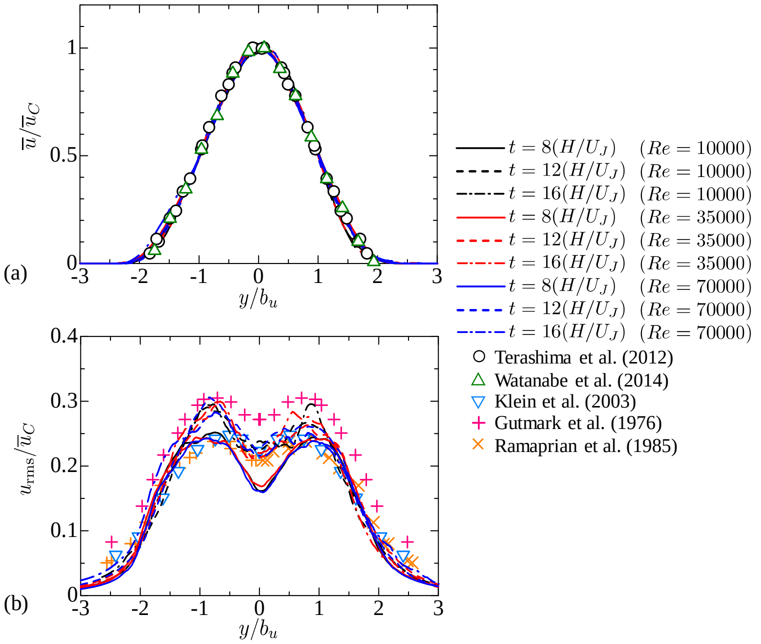

Figure 1: Lateral profiles of (a) mean streamwise velocity $\overline{u}$ and (b) rms streamwise velocity fluctuation u_{rms} at $t = 8(H/U_J)$, $12(H/U_J)$, and $16(H/U_J)$. $\overline{u}$ and u_{rms} are divided by the mean streamwise velocity on the centerline $\overline{u}_C$ while y is also divided by the jet half width b_u. The present DNS results are compared with experiments[54,7,55,56] and DNS[57] of spatially-evolving planar jets.

diffusion process.[53] The initial scalar profile is given by

$$\phi = \frac{1}{2}\phi_J + \frac{1}{2}\phi_J \tanh\left(\frac{H - 2|y|}{4\theta_J}\right), \tag{28}$$

where ϕ_J is the initial scalar value in the jet.

The governing equations, Eqs. (1), (2), and (3), are integrated with the finite difference code[26,58] based on the fractional step method, which uses a third-order Runge–Kutta method for temporal advancement and fully-conservative finite difference schemes[59] for spatial discretization. The grid

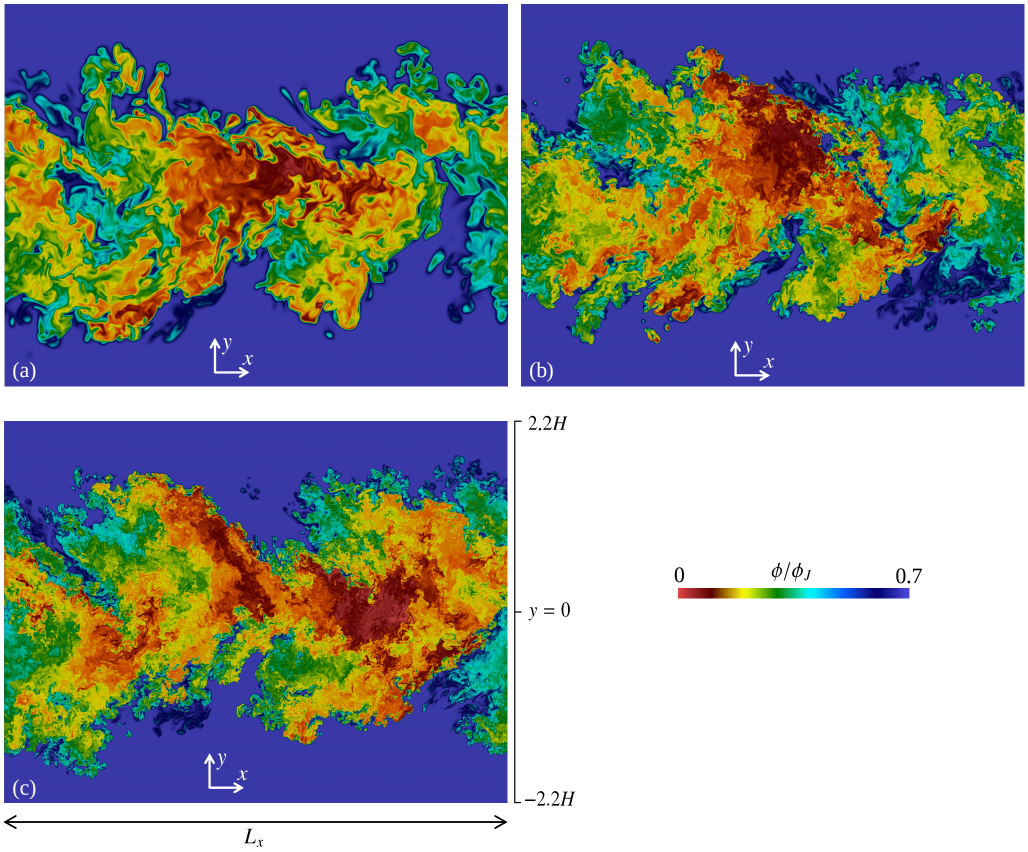

Figure 2: Color contour plots of passive scalar on a x-y plane at $t = 16(H/U_J)$ for (a) $Re = 10000$, (b) $Re = 35000$, and (c) $Re = 70000$.

Table 1: Statistical properties of planar jets at $t = 16(H/U_J)$. b_u and b_ϕ are jet half width based on mean profiles of streamwise velocity and passive scalar. η_C is Kolmogorov length scale, λ_C is Taylor microscale, and $Re_{\lambda C}$ is turbulent Reynolds number on the jet centerline.

Re	b_u	b_ϕ	η_C	λ_C	$Re_{\lambda C}$
10000	$0.88H$	$1.21H$	$4.2 \times 10^{-3}H$	$9.3 \times 10^{-2}H$	125
35000	$0.87H$	$1.19H$	$1.6 \times 10^{-3}H$	$4.7 \times 10^{-2}H$	205
70000	$0.81H$	$1.20H$	$0.9 \times 10^{-3}H$	$3.4 \times 10^{-2}H$	306

spacing is uniform in the homogeneous (x and z) directions while the grid is stretched in the lateral (y) direction near the boundaries. The fourth-order and second-order finite difference schemes are used in the x and z directions and y direction, respectively. The planar jet is simulated for three jet Reynolds numbers $Re = U_J H/\nu = 10000$, 35000, and 70000. The Schmidt number $Sc = \nu/D = 1$ in all simulations. The DNS is performed with the computational domain $(L_x, L_y, L_z) = (6H, 10H, 4H)$, which is represented by $(N_x \times N_y \times N_z)$ grid points, where $(N_x, N_y, N_z) = (1200, 1600, 800)$, $(2400, 3500, 1600)$, and $(4200, 5600, 2800)$ for $Re = 10000$, 35000, and 70000, respectively. Previous experiment and DNS of turbulent planar jets have shown that the auto-correlation function of streamwise velocity with streamwise separation distance reaches 0 around the distance of $2.5b_u$ (b_u: jet half width based on mean streamwise velocity).[60,57] The jet half width increases with time, and therefore L_x/b_u decreases as the jet grows. At the end of the present DNS ($t = 16H/U_J$), b_u has increased up to $L_x \approx 7b_u$, which is large enough for the temporal DNS to recover the theoretical scaling $b_u^2 \sim t$ as shown in previous study.[41]

Figure 1 shows the mean streamwise velocity $\overline{u}$ and rms velocity fluctuation $u_{rms} = (\overline{u'^2})^{1/2}$ divided by the centerline value of $\overline{u}$ denoted by $\overline{u}_C$ in comparison with experiments and DNS of spatially-evolving turbulent planar jets, where y is also divided by the jet half width b_u. The mean streamwise velocity has a typical profile in the self-similar region observed in previous experiments at $t = 8(H/U_J)$, and hardly changes with time. In contrast, $u_{rms}/\overline{u}_C$ for $|y/b_u| < 1$ increases from $t = 8(H/U_J)$ to $12(H/U_J)$, but $u_{rms}/\overline{u}_C$ has a similar profile for $t = 12(H/U_J)$ and $16(H/U_J)$. Thus, the temporally-evolving turbulent planar jets have fully developed at $t = 12(H/U_J)$.

Figure 2 visualizes the passive scalar on a x-y plane at $t = 16(H/U_J)$ for all Reynolds numbers. Smaller-scale structures appear as Re increases. Because of the initial condition of the scalar field, ϕ is equal to 0 in the non-turbulent region, where the scalar dissipation rate is also close to 0. Therefore, in the present study, the volumetric tensor model is tested for $0 \leq y \leq 2H$, where both turbulent and non-turbulent fluids are found.

Table 1 summarizes the turbulence characteristics at $t = 16(H/U_J)$. Here, b_ϕ is the jet half width based on the mean scalar $\overline{\phi}$, $\eta = (\nu^3/\overline{\varepsilon})^{1/4}$ is the Kolmogorov length scale, $\lambda = (\overline{u'^2}/\overline{(\partial u'/\partial x)^2})^{1/2}$ is the Taylor microscale, and $Re_\lambda = \sqrt{\overline{u'^2}}\lambda/\nu$ is the turbulent Reynolds number, where the subscript C refers a value on the jet centerline. The jet half width hardly depends on the Reynolds number while the Kolmogorov length scale decreases as Re increases. In all DNS, the grid spacing is smaller than $1.5\eta_C$ in the turbulent region.

4.2. Procedure for a priori test

The multi-particle model for the coarse-grained scalar dissipation rate is tested with the DNS database of the planar jet at $t = 16(H/U_J)$, at which the jet is fully developed. The following procedure is used in a priori test:

1. The number of particles N_M is determined.
2. N_M particles are randomly placed within a spherical volume with radius R_S whose center is located at (x_s, y_s, z_s).
3. The variables computed on the grid in the DNS are interpolated onto N_M particles with a tri-linear interpolation.
4. The volumetric tensor is computed based on the particle positions.
5. The coarse-grained scalar dissipation rate is computed with the multi-particle model Eq. (17) and with the ensemble average of scalar dissipation rate interpolated from the DNS grid.

The same procedure is repeated by changing (x_s, y_s, z_s), N_M, and R_S. The coarse-grained scalar dissipation rate estimated from Eq. (17) with the volumetric tensor is denoted by $\langle \varepsilon_\phi | V_M^n \rangle_{VT}$ while the one computed based on the DNS value of ε_ϕ is denoted by $\langle \varepsilon_\phi | V_M^n \rangle_{DNS}$. The relation between $\langle \varepsilon_\phi | V_M^n \rangle_{VT}$ and $\langle \varepsilon_\phi | V_M^n \rangle_{DNS}$ is investigated with the statistics computed with the ensemble average of the spheres whose center is located at the same y_s.

4.3. Results and discussion

Figure 3 shows probability density functions (PDFs) of elongation E and planarity P for N_M randomly distributed particles. As N_M decreases from $N_M \approx 10$ to 4, the probability for large E and P increases. In this case,

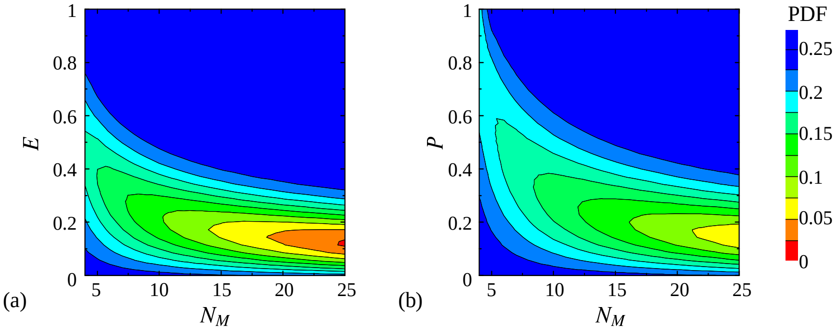

Figure 3: Probability density functions (PDF) of (a) elongation E and (b) planarity P computed as a function of the number of particles N_M.

the particle distribution is flat or elongated in one direction. For larger N_M, the PDFs are large for $0 \leq E \leq 0.3$ and $0 \leq P \leq 0.3$, and the particle distribution tends to be more isotropic.

Figures 4(a-c) show contour plots of averaged values of $C_{\varepsilon\phi}$ given by Eq. (18), $\overline{C_{\varepsilon\phi}}$, computed for $6 \leq N_M \leq 24$ and $1 \leq R_S/\eta_C \leq 250$. $\overline{C_{\varepsilon\phi}}$ increases with R_S. but weakly depends on N_M. This is because R_S is related to the cutoff length of the low-pass filter defined as the volume average, and the contribution from unresolved small scales to $\langle\varepsilon_\phi|V_M^n\rangle$ becomes greater as R_S becomes large. Magnitude of $\overline{C_{\varepsilon\phi}}$ reaches $O(10^2)$ when R_S exceeds $100\eta_C$. Figures 4(d-f) show color contour plots of $\overline{C_{\varepsilon\phi}}$ for small R_S. When $R_S \sim \eta_C$, the gradient estimation with the volumetric tensor yields a fully-resolved scalar gradient,[31] and $D\langle\partial\phi/\partial x_j|V_M^n\rangle\langle\partial\phi/\partial x_j|V_M^n\rangle$ is close to $\varepsilon_\phi = D\nabla\phi\cdot\nabla\phi$. Therefore, $C_{\varepsilon\phi}$ approaches 1 as R_S/η_C decreases to 1 as seen in Figs. 4(d-f).

Figure 5 compares averages of coarse-grained scalar dissipation rate, $\overline{\langle\varepsilon_\phi|V_M^n\rangle_{DNS}}$ and $\overline{\langle\varepsilon_\phi|V_M^n\rangle_{VT}}$, by plotting $R_\phi \equiv \overline{\langle\varepsilon_\phi|V_M^n\rangle_{DNS}}/\overline{\langle\varepsilon_\phi|V_M^n\rangle_{VT}}$ as a function of

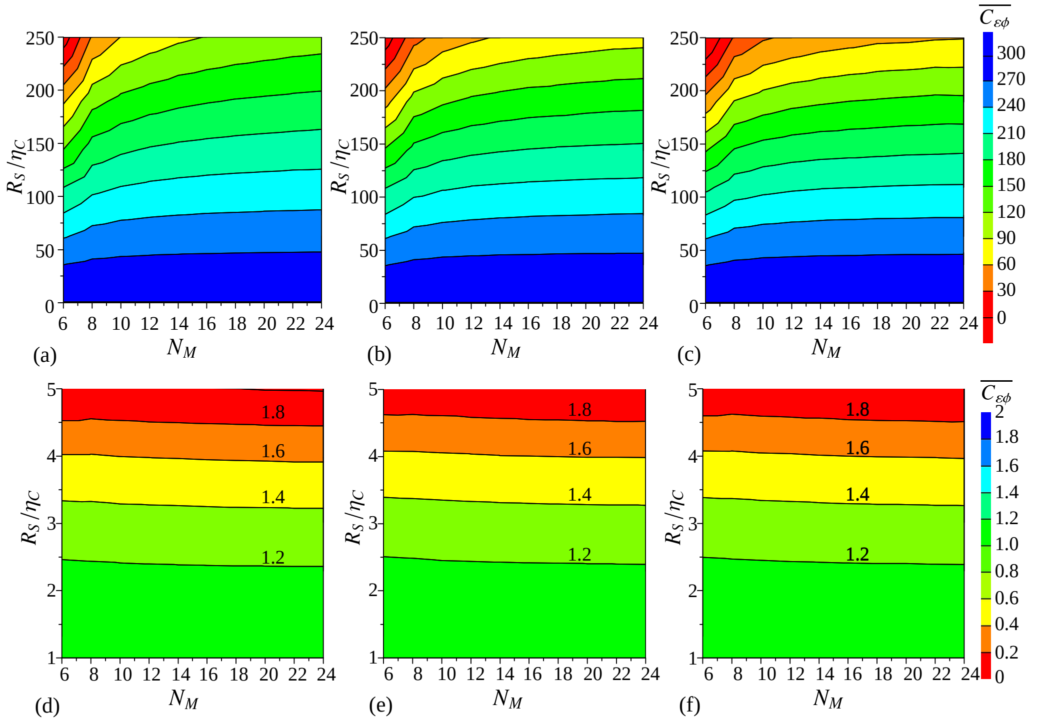

Figure 4: Averaged values of $C_{\varepsilon\phi}$ ($\overline{C_{\varepsilon\phi}}$) plotted against $(N_M, R_S/\eta_C)$ at $t = 16(H/U_J)$ on the centerline: (a) $Re = 10000$; (b) $Re = 35000$; (c) $Re = 70000$. $\overline{C_{\varepsilon\phi}}$ for $1 \le R_S/\eta_C \le 5$ is shown in (d-f): (d) $Re = 10000$; (e) $Re = 35000$; (f) $Re = 70000$.

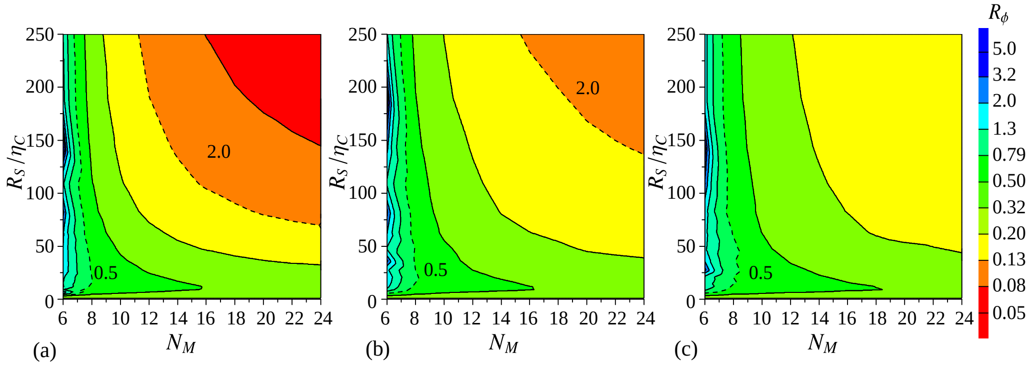

Figure 5: $R_\phi \equiv \overline{\langle \varepsilon_\phi | V_M^n \rangle_{DNS}} / \overline{\langle \varepsilon_\phi | V_M^n \rangle_{VT}}$ plotted against $(N_M, R_S/\eta_C)$ at $t = 16(H/U_J)$ on the centerline: (a) $Re = 10000$; (b) $Re = 35000$; (c) $Re = 70000$. Broken lines denote $R_\phi = 0.5$ and 2.0.

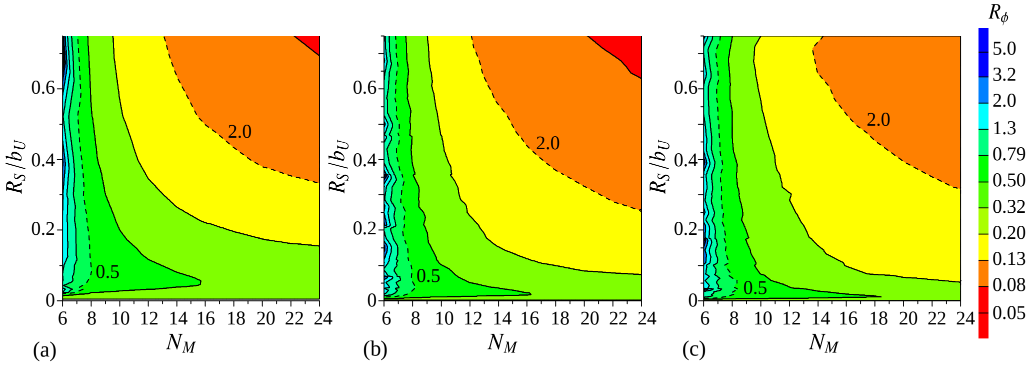

Figure 6: $R_\phi \equiv \overline{\langle \varepsilon_\phi | V_M^n \rangle_{DNS}} / \overline{\langle \varepsilon_\phi | V_M^n \rangle_{VT}}$ plotted against $(N_M, R_S/b_u)$ at $t = 16(H/U_J)$ on the centerline: (a) $Re = 10000$; (b) $Re = 35000$; (c) $Re = 70000$. Broken lines denote $R_\phi = 0.5$ and 2.0.

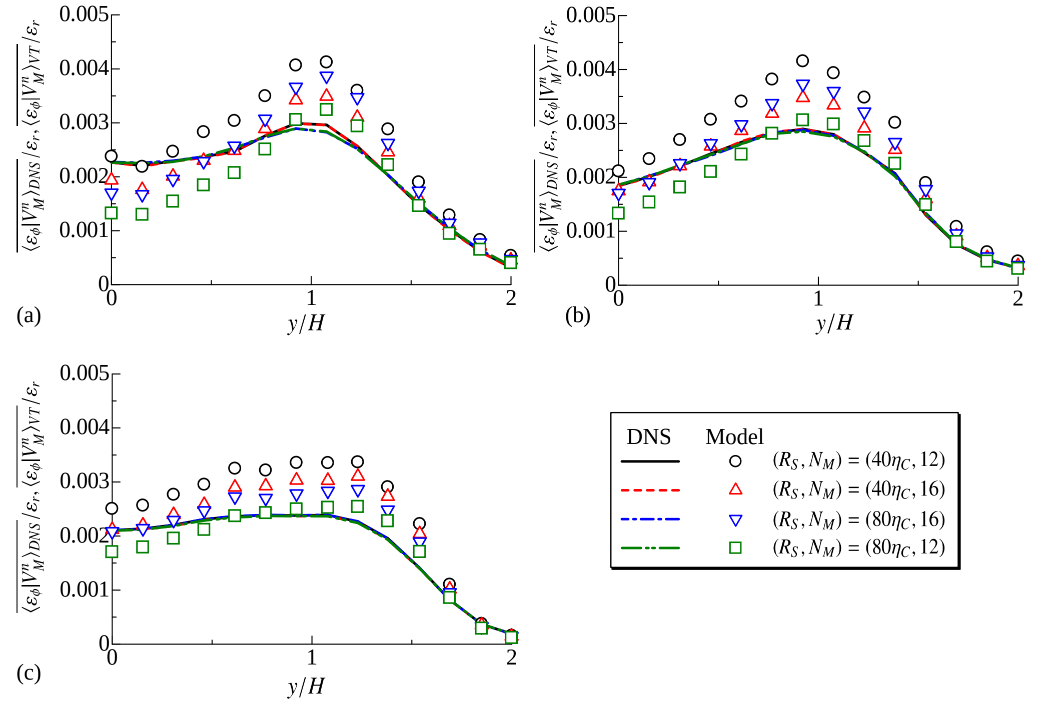

Figure 7: Lateral profiles of averaged coarse-grained scalar dissipation rate ($\overline{\langle \varepsilon_\phi | V_M^n \rangle_{DNS}}$ and $\overline{\langle \varepsilon_\phi | V_M^n \rangle_{VT}}$) at $t = 16(H/U_J)$: (a) $Re = 10000$; (b) $Re = 35000$; (c) $Re = 70000$. The coarse-grained scalar dissipation rate is normalized by $\varepsilon_r = \phi_J^2 U_J / H$.

$(N_M, R_S/\eta_C)$, where $R_\phi = 0.5$ and 2.0 are shown with broken lines. For most values of (N_M, R_S), R_ϕ has a value between 0.5 and 2.0. Thus, $\overline{\langle \varepsilon_\phi | V_M^n \rangle_{VT}}$ is of the same order of magnitude as the DNS value despite the strong dependence of $C_{\varepsilon\phi}$ on R_S in Fig. 4. However, the volumetric tensor model overestimates $\langle \varepsilon_\phi | V_M^n \rangle$ for small N_M as attested by $R_\phi \ll 1$ for $N_M \lesssim 8$. This is explained by an inaccurate estimation of the coarse-grained gradient $\langle \partial f/\partial x_j | V_M^n \rangle$ by the volumetric tensor for small N_M.[31] It is also found that R_ϕ has only a weak dependence on R_S for $N_M \lesssim 16$. Figure 6 shows R_ϕ against $(N_M, R_S/b_u)$. R_ϕ has a very similar profile for all Reynolds numbers when it is plotted with R_S/b_u. Dependence on Re in Fig. 6 is clearly seen for small R_S/b_u ($R_S/b_u \le 0.1$). For small R_S, R_ϕ for three Reynolds numbers is similar to each other when R_S is normalized by η_C in Fig. 5. The coarse-grained scalar dissipation rate $\langle \varepsilon_\phi | V_M^n \rangle$ with small R_S is close to the dissipation rate ε_ϕ in the fully resolved field, where the strongly-dissipative region has a sheetlike structure whose thickness is characterized by the Kolmogorov scale in the case of $Sc = 1$.[61,62] Therefore, the performance of the multi-particle model with small R_S depends on the Kolmogorov scale. On the other hand, the coarse-grained scalar gradient $\langle \partial\phi/\partial x_j | V_M^n \rangle$ for large R_S is related to the mean scalar gradient, which is characterized by the jet half width b_u. Therefore, R_ϕ with large R_S has a similar profile for all Reynolds number when R_S is normalized by b_u.

For large N_M, R_ϕ with large R_S/b_u exceeds 2, and the model underestimates the coarse-grained scalar dissipation rate. As N_M becomes large, the ensemble average of particles $\langle f | V_M^n \rangle$ approaches to the volume average because of the large number of samples in the volume V_M^n. Therefore,

$\langle \partial\phi/\partial x_j | V_M^n \rangle$ with large R_S and N_M is very close to 0 on the centerline because of the symmetric mean scalar profile in the planar jet. Nevertheless, $\langle \varepsilon_\phi | V_M^n \rangle$ does not approach 0 even if R_S increases. Because of this difference between $\langle \partial\phi/\partial x_j | V_M^n \rangle$ and $\langle \varepsilon_\phi | V_M^n \rangle$, the volumetric tensor model tends to underestimate $\langle \varepsilon_\phi | V_M^n \rangle$ when R_S/b_u and N_M are large. However, if N_M is small, $\langle \partial\phi/\partial x_j | V_M^n \rangle$ has a non-zero value because of the small number of samples in computing the ensemble average of particles. Therefore, the model does not work well with large N_M when R_S is as large as b_u.

Figure 7 shows lateral profiles of averaged coarse-grained scalar dissipation rate $\overline{\langle \varepsilon_\phi | V_M^n \rangle_{DNS}}$ and $\overline{\langle \varepsilon_\phi | V_M^n \rangle_{VT}}$ computed for $N_M = 12$ or 16 and $R_S = 40\eta_C$ or $80\eta_C$. The averaged coarse-grained scalar dissipation rate becomes small with y for $y/H \geq 1$, consistent with the DNS, since the scalar dissipation rate is very small in the non-turbulent region.[63,64] For all Reynolds numbers, the volumetric tensor model yields $\overline{\langle \varepsilon_\phi | V_M^n \rangle_{VT}}$ similar to $\overline{\langle \varepsilon_\phi | V_M^n \rangle_{DNS}}$. The profile of $\overline{\langle \varepsilon_\phi | V_M^n \rangle_{VT}}$ obtained with $N_M = 16$ is similar for both $R_S = 40\eta_C$ and $80\eta_C$ while dependence on R_S is more significant for $N_M = 12$ than $N_M = 16$. Nevertheless, the volumetric tensor model well estimates the order of magnitude of $\overline{\langle \varepsilon_\phi | V_M^n \rangle}$ for different sets of N_M and R_S. Even though the coefficient $C_{\varepsilon\phi}$ varies in the range of $O(10^0)$-$O(10^2)$ depending on N_M and R_S, magnitude of $\overline{\langle \varepsilon_\phi | V_M^n \rangle}$ is not sensitive to N_M and R_S, and the estimation of the coarse-grained scalar dissipation rate only weakly depends on these parameters.

5. LES-Lagrangian particle simulations of passive scalar mixing in planar jets

5.1. Implementation of the coarse-grained scalar dissipation model

The multi-particle model of coarse-grained scalar dissipation based on the volumetric tensor is applied to the LES/LPS, where the passive scalar is treated with Lagrangian notional particles. The LES solves Eqs. (4) and (5), where the velocity $\tilde{\mathbf{u}}$ is interpolated onto particle positions providing $\tilde{\mathbf{u}}^{(n)}(t)$ for solving Eq. (6) for N_P particles. The MVM is applied for Eq. (7) with V_M^n that contains N_M mixing particles, where N_M is treated as a computational parameter in the simulation. For particle n, $N_M - 1$ mixing particles are selected at every computational time step in the descending order according to the distance from particle n. With integer $\alpha = 1, ..., N_M$ that represents the particles within V_M^n, the MVM for particle n is applied in the form of

$$\frac{d\phi^{(\alpha)}}{dt} = \frac{1}{N_M \tau_M} \left(\langle \phi | V_M^n \rangle - \phi^{(\alpha)} \right) \quad \text{for } \alpha = 1, ..., N_M, \tag{29}$$

with τ_M computed by Eq. (12) with the multi-particle model for $\langle \varepsilon_\phi | V_M^n \rangle$. The MVM applied for particle n affects N_M particles within V_M^n by Eq. (29). For every computational time step, the mixing volume is set up for all of N_P particles, and Eq. (29) is computed for all mixing volumes. The MVM is sequentially applied from $n = 1$ to N_P. Because the initial position of particles is randomly chosen, there is no specific order in computation of the MVM. The present method allows one particle to participate more than one mixing event, where $\phi^{(n)}$ can be modified more than once in one computational time step. τ_M is defined so that one event decays the scalar variance within the mixing volume at the coarse-grained scalar dissipation rate. One mixing particle participates N_M mixing events on average per one computational time step. Therefore, τ_M in Eq. (9) is replaced by $N_M\tau_M$ in Eq. (29) so that the MVM computed for all particles provides a correct decay rate of the scalar variance.

5.2. Numerical methods

The LES/LPS is used for simulating the temporally-evolving planar jet with passive scalar transfer considered in the DNS. The LES is performed with the same finite difference code as in the DNS used for a priori test. The difference in the LES code from the DNS is in the influences of unresolved scales, which appear as R_i in the governing equations described by Eqs. (4) and (5). We use an implicit LES (ILES) that relies on a numerical low-pass filter which mimics kinetic energy dissipation in unresolved scales. In the present study, an explicit tenth-order low-pass filter[65] is applied to all components of the velocity vector at the end of every computational time step. Therefore, R_i in Eq. (5) is implicitly treated in the simulations. Our previous study has confirmed that the velocity statistics in the ILES of planar jets agree with the DNS.[36,26]

The detail of the LPS is documented below. Initially, N_P particles are randomly placed in the computational domain. The initial scalar value $\phi^{(n)}$ is given by substituting $y = y^{(n)}$ to Eq. (28). The resolved velocity $\tilde{\mathbf{u}}$ in the LES is interpolated onto the particle positions with the tri-linear interpolation. Equation (6) is integrated with the first-order Euler scheme, which is also used for Eq. (7) unless the time increment Δt is larger than $N_M\tau_M$. When $\Delta t > N_M\tau_M$, the scalar values of the particles within the mixing volume are replaced by the mean value within the mixing volume $\langle\phi|V_M^n\rangle$ instead of

Table 2: Computational parameters in the LES/LPS. η_C is taken at $t = 16(H/U_J)$.

	Re	N_P	N_M	R_{MV}/η_C	ρ_P
Case 1	10000	30000	12	68	$125H^{-3}$
Case 2	10000	60000	12	54	$250H^{-3}$
Case 3	35000	10000	8	217	$41.7H^{-3}$
Case 4	35000	10000	12	249	$41.7H^{-3}$
Case 5	35000	30000	12	172	$125H^{-3}$
Case 6	35000	30000	24	217	$125H^{-3}$
Case 7	35000	60000	12	137	$250H^{-3}$
Case 8	35000	60000	24	172	$250H^{-3}$
Case 9	70000	30000	12	289	$125H^{-3}$
Case 10	70000	60000	12	230	$250H^{-3}$

using Eq. (7).

The MVM needs to calculate the distance among particles for selecting the mixing particles. Calculation of the distance for all possible particle pairs takes long computation time. In the present simulation, the candidate of mixing particles is chosen by dividing the computational domain into small subdomains each of which contains approximately $10N_M$ particles. The distance between two particles is computed for particle pairs located in the same subdomain. The mixing particles close to particle n are selected from the subdomain with the bubble sort algorithm.

5.3. Computational parameters

The LES/LPS uses the computational domain of $(L_x, L_y, L_z) = (6H, 10H, 4H)$, which is the same as the DNS. The number of grid points in the LES is $(N_x, N_y, N_z) = (120, 180, 80)$ for all Reynolds numbers: $Re = 10000, 35000$, and 70000. The non-uniform grid is used only in the lateral (y) direction. The LES/LPS is performed with 10 sets of the parameters (Re, N_P, N_M) as summarized in Tab. 2. $\rho_P = N_P/L_xL_yL_z$ is the number density of particles, and $R_{MV} = (3N_M/4\pi\rho_P)^{1/3}$ gives the estimate of the order of the typical mixing volume size. Here, R_{MV} is divided by η_C taken from the DNS at $t = 16(H/U_J)$. Note that the size of each mixing volume is given from the volumetric tensor. The value of N_P is selected based on R_{MV} to investigate the influence of the mixing volume size.

In the next subsection, cases 3-8 with $Re = 35000$ are used for investigating the influences of the parameters in the MVM: the influences of N_M are discussed by comparing cases 3 and 5 with 6 and 8, respectively, for the same values of R_{MV}; the dependence on R_{MV} at the same N_M is discussed from cases 4, 5, and 7 for $N_M = 12$ and cases 6 and 8 for $N_M = 24$. The Reynolds number dependence is also studied from cases 1, 2, 5, 7, 9, and 10, for which $(N_P, N_M) = (30000, 12)$ or $(60000, 12)$.

The statistics in the LPS are computed by ensemble averages of particles[23,26] as illustrated in Fig. 8. In the temporally-developing planar jets, the statistics are represented as a function of y and time t. For computing the statistics in the LPS, the y coordinate is divided into 180 regions, each of which has the length of $\Delta_y = L_y/180$. jth region ($j = 1, ..., 180$) is located for $(j-1)\Delta_y \leq y < j\Delta_y$. The particle in $(j-1)\Delta_y \leq y^{(n)}(t) < j\Delta_y$ is used

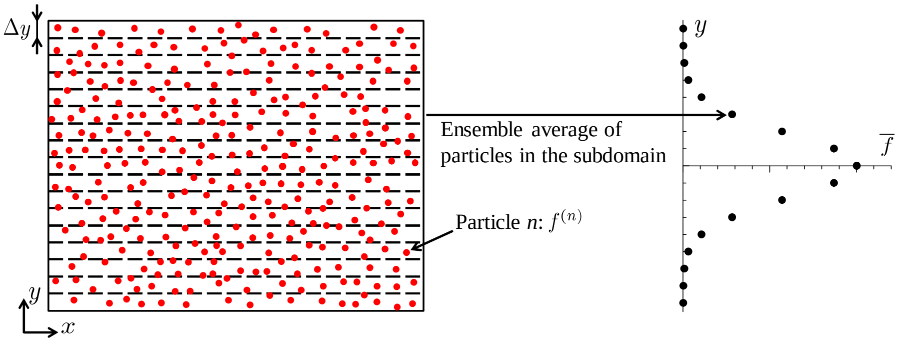

Figure 8: Computation of statistics from particles.

as a sample for ensemble averages in the jth region. The statistics in the jth region are presented against the center location $(2j-1)\Delta_y/2$. The degree of statistical convergence depends on the number of particles. The LES/LPS with each set of parameters is repeated 180 times with different initial positions of particles. 180 times of the simulations are used for computing statistics in order to reduce statistical uncertainty.

For case 1, the computation time of the LES/LPS is about 1/1000 times of that of the DNS, where the computation time was measured with the high-performance computing system, CX100, in Nagoya University. The computation time of the LES/LPS is significantly affected by the number of grid points in the LES and the number of particles in the LPS. The number of grid points in the LES is determined based on large scales of turbulent flows, and hardly increases with the jet Reynolds number. On the other hand, more grid points are required in the DNS at higher Reynolds number. Therefore, the difference in the computation time between the LES/LPS and the DNS increases with the Reynolds number.

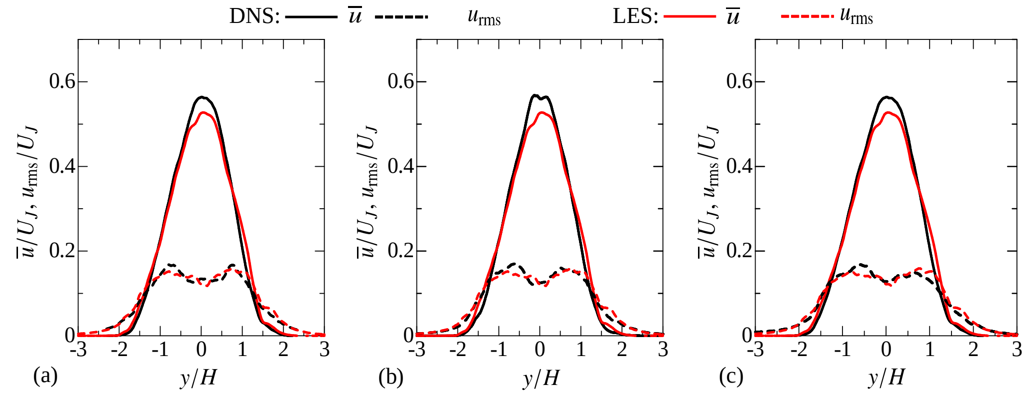

Figure 9: Lateral profiles of mean streamwise velocity and rms streamwise velocity fluctuation at $t = 16(H/U_J)$: (a) $Re = 10000$; (b) $Re = 35000$; (c) $Re = 70000$.

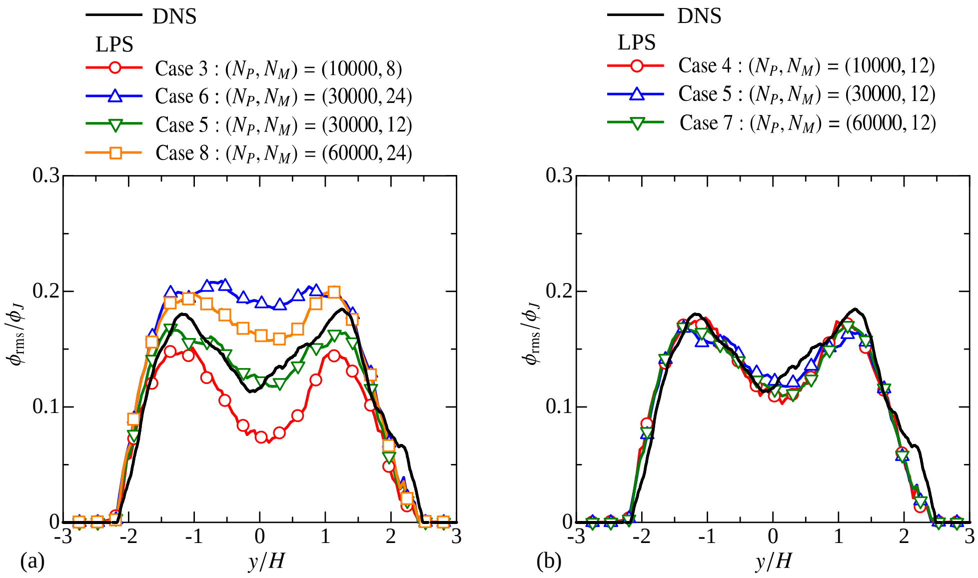

Figure 10: Rms values of ϕ', ϕ_{rms}, at $t = 16(H/U_J)$ for $Re = 35000$ in the LES/LPS and DNS: (a) cases 3, 5, 6, and 8; (b) cases 4, 5, and 7.

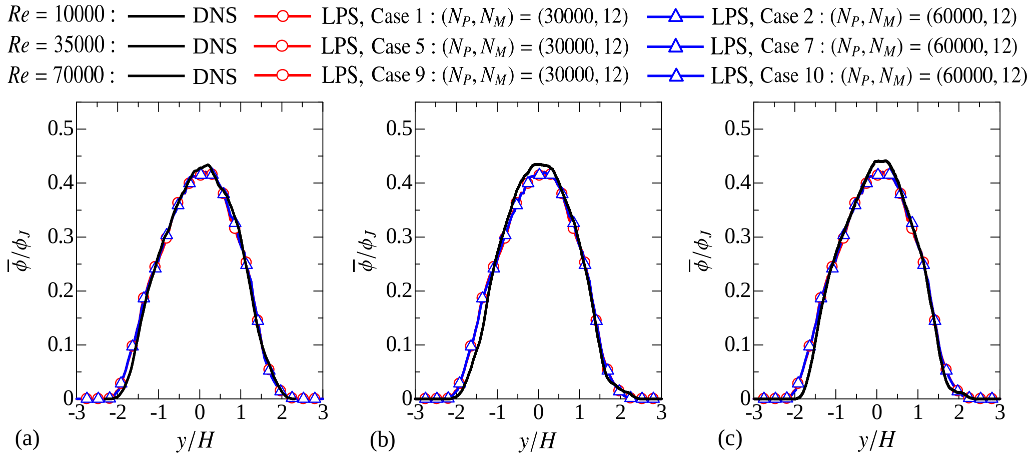

Figure 11: Mean values of ϕ at $t = 16(H/U_J)$ in the LES/LPS and DNS: (a) $Re = 10000$; (b) $Re = 35000$; (c) $Re = 70000$.

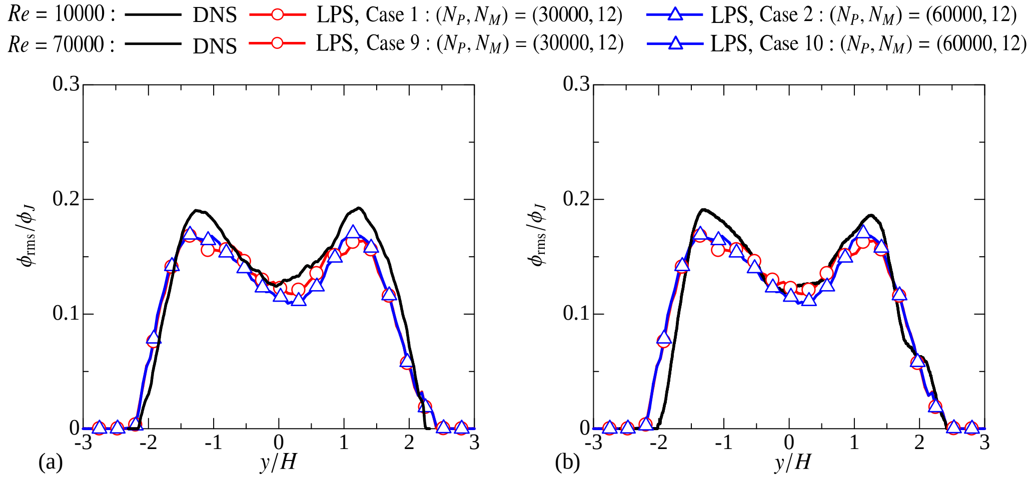

Figure 12: Re-dependence of rms values of ϕ', ϕ_{rms}, at $t = 16(H/U_J)$ in the LES/LPS and DNS: (a) $Re = 10000$; (b) $Re = 70000$.

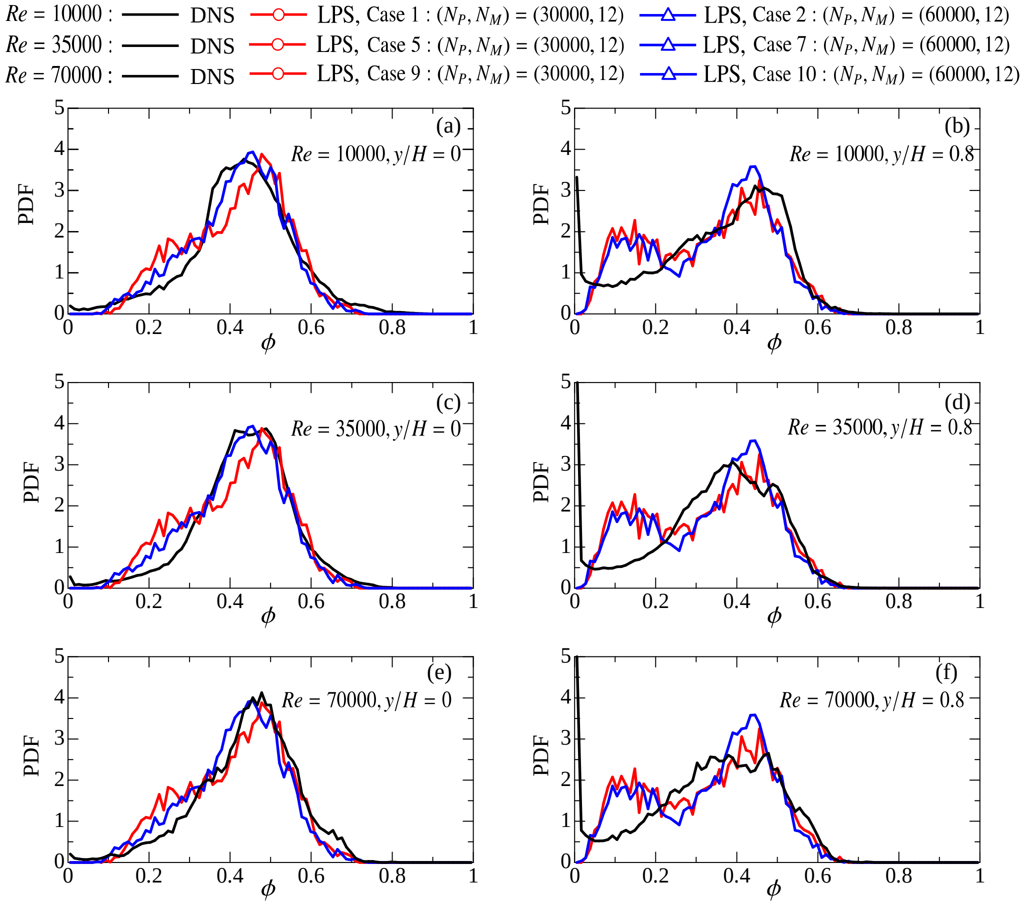

Figure 13: Probability density function of ϕ at $t = 16(H/U_J)$ in the LES/LPS and DNS: (a) $Re = 10000, y/H = 0$; (b) $Re = 10000, y/H = 0.8$; (c) $Re = 35000, y/H = 0$; (d) $Re = 35000, y/H = 0.8$; (e) $Re = 70000, y/H = 0$; (f) $Re = 70000, y/H = 0.8$.

5.4. Results and Discussion

The resolved velocity in the ILES is interpolated on the particle position. This particle velocity is important for accurate prediction of turbulent diffusion. Since the LES/LPS is evaluated by comparison with the DNS results, the velocity field in the ILES should be consistent with the reference DNS database. Figure 9 compares lateral profiles of mean streamwise velocity $\overline{u}$ and rms streamwise velocity fluctuation, u_{rms}, between the ILES and the DNS. Here, the statistics of the resolved velocity $\tilde{u}$ in the ILES are presented (i.e. $\overline{\tilde{u}}$ and $u_{\mathrm{rms}} = \sqrt{\overline{\tilde{u}^2} - \overline{\tilde{u}}^2}$). Both $\overline{u}$ and u_{rms} in the ILES agree well with the DNS for all Reynolds numbers since $\overline{u}$ and u_{rms} are governed by large scales in the jet and the contribution from the unresolved scale is small.

Figure 10 compares rms values of ϕ, $\phi_{\mathrm{rms}} = \sqrt{\overline{\phi'^2}}$, between the LES/LPS and the DNS for $Re = 35000$ at $t = 16(H/U_J)$. Figure 10(a) includes cases 3, 5, 6, and 8, where the characteristic radius of mixing volume is $R_{MV} = 217\eta_C$ in cases 3 and 6 and $R_{MV} = 172\eta_C$ in cases 5 and 8. Comparing these cases with the same R_{MV} indicates that ϕ_{rms} in the LES/LPS becomes larger as the number of mixing particles N_M increases. This tendency is clearer for $|y/H| \leq 1.5$, where the scalar dissipation rate is higher than the outer region ($|y/H| > 1.5$). For $|y/H| \leq 1.5$, ϕ_{rms} in the LES/LPS with $N_M = 24$ is larger than the DNS values. ϕ_{rms} is closely related to the modeled scalar dissipation rate, and smaller (larger) ϕ_{rms} is caused by larger (smaller) dissipation rate. The observed dependence on N_M agrees with a priori test in Figs. 5 and 6, which also show that the model with $N_M = 8$ and 24 overestimates and underestimates the scalar dissipation rate, respectively. Figure 10(b) compares ϕ_{rms} among the LES/LPS with $N_M = 12$ (cases 4, 5, and 7) and the DNS. These LES/LPS in Fig. 10(b) have the same N_M but different values of N_P, which results in a different size of the mixing volume (R_{MV}) as summarized in Tab. 2. At $N_M = 12$, the number of the particles N_P does not affect ϕ_{rms}, implying the present mixing model works well for $N_M = 12$ independently from the size of the mixing volume. Therefore, ϕ_{rms} shows a good agreement between the DNS and the LES/LPS. This is also expected from a priori test in Fig. 5, where the dependence of the present model on R_{MV} is weak around $N_M \approx 12$.

Figure 11 shows the mean profile of ϕ, $\overline{\phi}$, in the LES/LPS at $N_M = 12$ and the DNS. The DNS results of $\overline{\phi}$ hardly depend on the Reynolds number. This is expected from the mean scalar transport equation, obtained by taking an average of Eq. (3), where the turbulent transport term is more important than the molecular diffusion term, which is modeled by the MVM, except for very low Reynolds and Schmidt numbers. The Reynolds number in the present DNS is high enough for $\overline{\phi}$ to be almost independent of the Reynolds number. The LES/LPS with different R_{MV} predicts well $\overline{\phi}$ at all Reynolds numbers even though the MVM is applied with a large mixing volume in relation to the Kolmogorov scale.

Figures 12(a) and (b) show ϕ_{rms} for $Re = 10000$ and 70000, respectively, comparing the results from the LES/LPS at $N_M = 12$ and the DNS (cases 1 and 2 for $Re = 10000$; cases 9 and 10 for $Re = 70000$). The LES/LPS with $N_M = 12$ predicts ϕ_{rms} well even at these Reynolds numbers.

Figure 13 shows probability density function (PDF) of ϕ on the jet centerline (a,c,e) and at $y/H = 0.8$ (b,d,f) obtained from the LES/LPS and the DNS. Overall profiles of the PDF are well predicted by the LES/LPS on the jet centerline. However, the LES/LPS fails to predict the shape of the PDF at $y/H = 0.8$, where a large peak of the PDF at $\phi = 0$ in the DNS results cannot be seen in the LES/LPS results. This is because the MVM with a large mixing volume cannot accurately express the molecular diffusion in the intermittent region, where both turbulent and non-turbulent fluids coexist. The computational grid size in the DNS is small enough to accurately capture the intermittent distribution of turbulent ($\phi > 0$) and non-turbulent fluids ($\phi = 0$), and thus, a large peak of the PDF at $\phi = 0$ is obtained because the non-turbulent fluid with $\phi = 0$ exists at $y/H = 0.8$. In the intermittent region, there exists a thin interfacial layer that separates the turbulent from non-turbulent fluids, across which ϕ rapidly changes from $\phi = 0$ to $\phi > 0$ (also see the scalar field in Fig. 2).[66] This interfacial layer is called the turbulent and non-turbulent interfacial (TNTI) layer, where the molecular diffusion causes the scalar transfer between the turbulent and non-turbulent fluids.[67,64] It has been shown that the thickness of the TNTI layer is about 10 times of the Kolmogorov length scale.[67,68] The MVM with $R_{MV} \gg \eta$ cannot accurately express the molecular diffusion across the TNTI layer: such mixing with large R_{MV} changes the scalar value in the non-turbulent fluid far away from the turbulent region rather than in the proximity of the TNTI layer. This results in reduction of probability that the fluid with $\phi = 0$ is found in the intermittent region in the LES/LPS in Figs. 13(b,d,f). The volumetric tensor model uses the spectrum E_ϕ of turbulent flows even though the intermittent region is partially laminar. Despite these difficulties in the intermittent region, the LES/LPS can predicts the overall shape of the PDF of ϕ except the peak at $\phi = 0$ in Figs. 13(b,d,f).

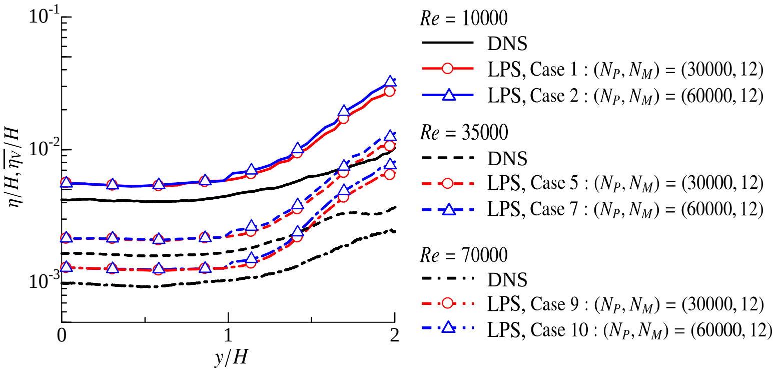

Figure 14: Lateral profiles of Kolmogorov scale predicted by Eq. (23) in the LES/LPS ($\overline{\eta_V}$) in comparison with the DNS results $\eta = (\nu^3/\bar{\varepsilon})^{1/4}$ at $t = 16(H/U_J)$.

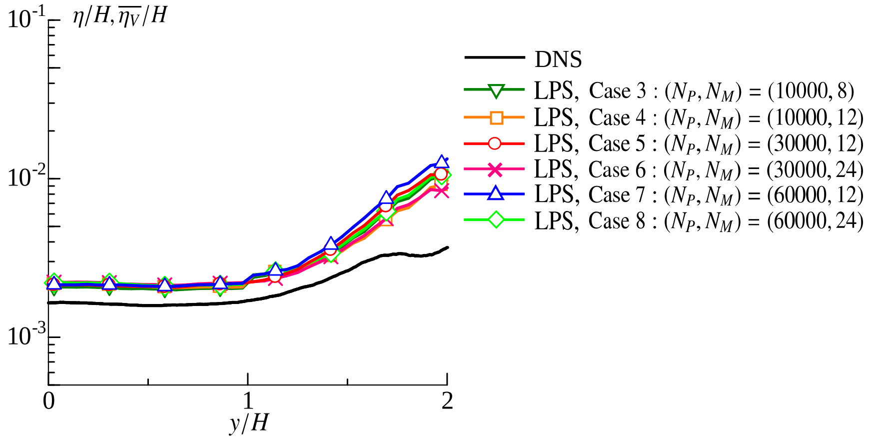

Figure 15: Lateral profiles of Kolmogorov scale predicted by Eq. (23) in the LES/LPS ($\overline{\eta_V}$) at $t = 16(H/U_J)$ for $Re = 35000$. The results are compared with η in the DNS.

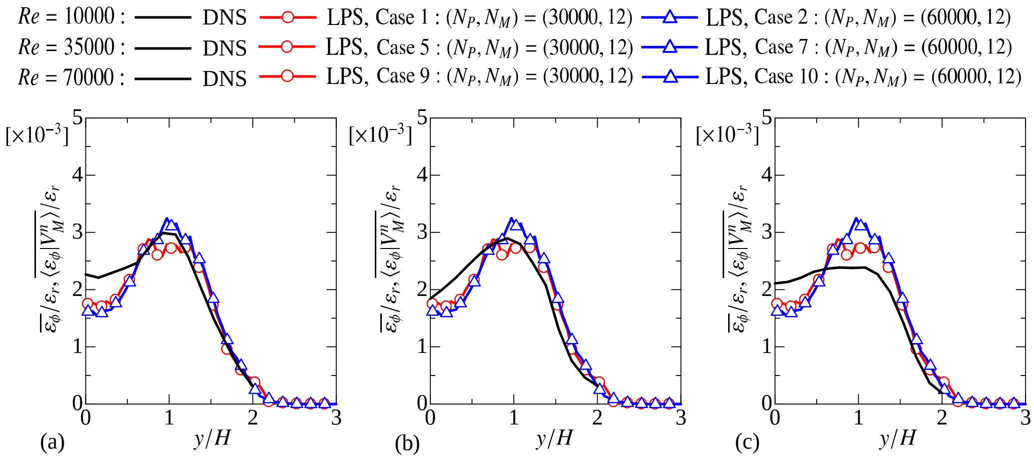

Figure 16: Comparison of mean scalar dissipation rate between the DNS ($\overline{\varepsilon_\phi}$) and LES/LPS ($\overline{\langle\varepsilon_\phi|V_M^n\rangle}$) at $t = 16(H/U_J)$: (a) $Re = 10000$; (b) $Re = 35000$; (c) $Re = 70000$. The scalar dissipation rate is normalized by $\varepsilon_r = \phi_J^2 U_J/H$.

A mixing volume is assigned to each particle in one computational time step, where the multi-particle model estimates the coarse-grained scalar dissipation rate $\langle\varepsilon_\phi|V_M^n\rangle$ for all mixing volumes. In this computation, the Kolmogorov length scale is also computed for each mixing volume as η_V in Eq. (23). $\langle\varepsilon_\phi|V_M^n\rangle$ and η_V computed for V_M^n are treated as the values assigned to particle n, and the averaged values $\overline{\langle\varepsilon_\phi|V_M^n\rangle}$ and $\overline{\eta_V}$ are computed with ensemble average of particles. Figure 14 compares the Kolmogorov scales $\overline{\eta_V}$ in the LES/LPS and $\eta = (\nu^3/\overline{\varepsilon})^{1/4}$ in the DNS in the region of $0 \leq y/H \leq 2$ at $t = 16(H/U_J)$. Both $\overline{\eta_V}$ and η hardly depend on y for $0 \leq y/H \leq 1$, while they increase in the y direction for $1 < y/H$ because the non-turbulent fluid with small kinetic energy dissipation rate exists in this region.[51] It is well known as one of the characteristics of turbulence that the Kolmogorov scale becomes smaller as Reynolds number becomes large. $\overline{\eta_V}$ in the LES/LPS also shows this tendency, and the Re dependence of the Kolmogorov scale is well captured by the LES/LPS. Although $\overline{\eta_V}$ in the LES/LPS is larger than η in the DNS, this difference is not large: $\overline{\eta_V}/\eta$ at $y = 0$ is $1.34, 1.30$, and 1.31 for Re = 10000, 35000, and 70000, respectively. Figure 15 compares the Kolmogorov scales in the LES/LPS and the DNS for $Re = 35000$. The Kolmogorov scale estimated in the LES/LPS, $\overline{\eta_V}$, hardly depends on the parameters (N_P, N_M). $\overline{\eta_V}$ is estimated based on the Re dependence of length scales by Eq. (23), which includes a coefficient of the order of 1. In Figs. 14 and 15, $\overline{\eta_V}$ in the LES/LPS is slightly larger than η in the DNS because of the present choice of the coefficient. Because the model spectrum computed with η_V is integrated in wavenumber space, the small difference between $\overline{\eta_V}$ and η is not important, and the LES/LPS well predicts the statistics of the planar jet as found in Figs. 10-13.

Figure 16 shows lateral profiles of $\overline{\langle \varepsilon_\phi | V_M^n \rangle}$ in the LES/LPS and $\overline{\varepsilon_\phi}$ in the DNS. Although the Kolmogorov scale estimated in the LES/LPS is slightly larger than the DNS value as shown in Fig. 14, mean values of the modeled coarse-grained scalar dissipation rate agree well with $\overline{\varepsilon_\phi}$ in the DNS. Thus, an exact value of the Kolmogorov scale does not have a significant influence on the coarse-grained scalar dissipation rate as long as the order of the scale is well estimated by Eq. (23). This is because the dissipation spectrum $k^2 E_\phi(k)$ used in Eq. (18) peaks at k smaller than the wavenumber corresponding to the Kolmogorov scale.

6. Conclusion

The multi-particle model for coarse-grained scalar dissipation rate, defined as the local volume average of scalar dissipation rate, is developed based on the volumetric tensor estimation of coarse-grained gradient[31] and the SGS model of scalar dissipation rate.[29] Here, the volumetric tensor is used for computing the coarse-grained gradient of scalar and velocity from the particle field and for estimating the length scale of the particle distribution, while the SGS model is required to estimate the coarse-grained scalar dissipation rate from the coarse-grained scalar gradient, which does not contain the contribution from scales smaller than the length scale of the particle distribution. The present model enables us to directly compute the coarse-grained scalar dissipation rate from spatially-distributed notional particles, which are often used in Lagrangian particle simulations (LPS) of turbulent reacting flows. The proposed model is examined with both a priori and posteriori tests.

A priori test is performed with the DNS database of turbulent planar jets. It is found that the multi-particle model overestimates the coarse-grained scalar dissipation rate when less than 8 particles are used in the model. The model performance is examined for a wide range of the length scale that characterizes the particle distribution. It is shown that the model prediction depends on the particle-distribution length scale normalized by the Kolmogorov scale η when magnitudes of these scales are comparable to each other. In contrast, length scales of large scales in a flow, such as jet half width, become important in the model performance when the particle-distribution length scale is much larger than η. Note that these are obtained for $Sc = 1$, and η in the above discussion needs to be replaced by another length scale that characterizes the smallest scale of scalar fluctuation. When the number of the particles used in the model is between 10 and 16, the multi-particle model well predicts the coarse-grained scalar dissipation rate in the turbulent jet for a wide range of the particle-distribution length scale.

The multi-particle model with the volumetric tensor is implemented in the LES/LPS with the mixing volume model (MVM) for molecular diffusion, where the coarse-grained scalar dissipation rate $\langle \varepsilon_\phi | V_M^n \rangle$, defined as the volume average of ε_ϕ within the mixing volume V_M^n, appears as an unknown variable. Here, N_M particles within the mixing volume are used for estimating $\langle \varepsilon_\phi | V_M^n \rangle$ with the multi-particle model. The LES/LPS is used to simulate the turbulent planar jet, where the results are compared with the DNS. The computation time of the LES/LPS is less than 1/1000 times of that of the DNS, where the difference in the computation time between the LES/LPS and the DNS increases with the jet Reynolds number. The LES/LPS with the MVM and the multi-particle model of $\langle \varepsilon_\phi | V_M^n \rangle$ well predicts rms values of scalar fluctuations, indicating that the coarse-grained scalar dissipation rate is well estimated by the present model. As also expected from a priori test, a better agreement between the LES/LPS and the DNS is found for $N_M = 12$ than for $N_M = 8$ and 24. The LES/LPS also predicts well the PDF of passive scalar on the jet centerline, while the shape of the PDF in the intermittent region of turbulent jet is slightly different between the LES/LPS and the DNS. The MVM with large mixing volume changes the scalar value in the non-turbulent region although this does not occur in the DNS, where the PDF in the intermittent region has a large peak for the scalar value in the non-turbulent region. The Kolmogorov scale and averaged coarse-grained scalar dissipation rate estimated by the present model are consistent with the DNS results. Thus, it is confirmed that the multi-particle model well estimates the coarse-grained scalar dissipation rate in the context of the LES/LPS with the MVM. The present multi-particle model is useful in application of LES to turbulent reacting flows because the LPS combined with the LES does not require SGS models for chemical reaction rates unlike in a simple LES computing both velocity and reactive scalars.

Acknowledgment

The direct numerical simulations presented in this manuscript were carried out on the high-performance computing system (NEC SX-ACE) in the Japan Agency for Marine-Earth Science and Technology. This work was partially supported by "Collaborative Research Project on Computer Science with High-Performance Computing in Nagoya University" and by MEXT KAKENHI Grant Number 18K13682 and 18H01367.

References

[1] J. C. Hill, Homogeneous turbulent mixing with chemical reaction, Annu. Rev. Fluid Mech. 8 (1976) 135–161.

[2] J. Zhang, S. Xu, W. Li, High shear mixers: A review of typical applications and studies on power draw, flow pattern, energy dissipation and transfer properties, Chem. Eng. Process. 57 (2012) 25–41.

[3] R. W. Bilger, L. R. Saetran, L. V. Krishnamoorthy, Reaction in a scalar mixing layer, J. Fluid Mech. 233 (1991) 211–242.

[4] S. Komori, T. Kanzaki, Y. Murakami, Concentration correlation in a turbulent mixing layer with chemical reactions, J. Chem. Eng. Jpn. 27 (6) (1994) 742–748.

[5] V. Zhdanov, A. Chorny, Development of macro-and micromixing in confined flows of reactive fluids, Int. J. Heat Mass Transfer 54 (15) (2011) 3245–3255.

[6] A. Chorny, V. Zhdanov, Turbulent mixing and fast chemical reaction in the confined jet flow at large Schmidt number, Chem. Eng. Sci. 68 (1) (2012) 541–554.

[7] T. Watanabe, Y. Sakai, K. Nagata, O. Terashima, Experimental study on the reaction rate of a second-order chemical reaction in a planar liquid jet, AIChE J. 60 (11) (2014) 3969–3988.

[8] T. Michioka, S. Komori, Large-eddy simulation of a turbulent reacting liquid flow, AIChE J. 50 (11) (2004) 2705–2720.

[9] U. Schumann, Large-eddy simulation of turbulent diffusion with chemical reactions in the convective boundary layer, Atmos. Environ. 23 (8) (1989) 1713–1727.

[10] A. Y. Klimenko, R. W. Bilger, Conditional moment closure for turbulent combustion, Prog. Energy Combust. Sci. 25 (6) (1999) 595–687.

[11] P. J. Colucci, F. A. Jaberi, P. Givi, S. B. Pope, Filtered density function for large eddy simulation of turbulent reacting flows, Phys. Fluids 10 (1998) 499.

[12] H. Pitsch, Large-eddy simulation of turbulent combustion, Annu. Rev. Fluid Mech. 38 (2006) 453–482.

[13] A. Y. Klimenko, On simulating scalar transport by mixing between Lagrangian particles, Phys. Fluids 19 (3) (2007) 031702.

[14] A. Y. Klimenko, Lagrangian particles with mixing. II. Sparse-Lagrangian methods in application for turbulent reacting flows, Phys. Fluids 21 (6) (2009) 065102.

[15] C. Le Ribault, S. Simoëns, I. Vinkovic, Hybrid large eddy simulation/Lagrangian stochastic model for turbulent passive and reactive scalar dispersion in a plane jet, Chem. Eng. Commun. 199 (4) (2012) 435–460.

[16] T. Watanabe, K. Nagata, LES–Lagrangian-particles-simulation of turbulent reactive flows at high Sc number using approximate deconvolution model, AIChE J. 62 (8) (2016) 2912–2922.

[17] C. Marchioli, M. V. Salvetti, A. Soldati, Some issues concerning large-eddy simulation of inertial particle dispersion in turbulent bounded flows, Phys. Fluids 20 (4) (2008) 040603.

[18] J.-P. Minier, S. Chibbaro, S. B. Pope, Guidelines for the formulation of Lagrangian stochastic models for particle simulations of single-phase and dispersed two-phase turbulent flows, Phys. Fluids 26 (11) (2014) 113303.

[19] A. Innocenti, C. Marchioli, S. Chibbaro, Lagrangian filtered density

function for LES-based stochastic modelling of turbulent particle-laden flows, Phys. Fluids 28 (11) (2016) 115106.

[20] R. L. Curl, Dispersed phase mixing: I. Theory and effects in simple reactors, AIChE J. 9 (2) (1963) 175–181.

[21] C. Dopazo, E. E. O'Brien, An approach to the autoignition of a turbulent mixture, Acta Astronaut. 1 (9) (1974) 1239–1266.

[22] A. Y. Klimenko, S. B. Pope, The modeling of turbulent reactive flows based on multiple mapping conditioning, Phys. Fluids 15 (7) (2003) 1907–1925.

[23] R. O. Fox, Computational Models for Turbulent Reacting Flows, Cambridge Univ. Pr., 2003.

[24] D. W. Meyer, A new particle interaction mixing model for turbulent dispersion and turbulent reactive flows, Phys. Fluids 22 (3) (2010) 035103.

[25] T. Watanabe, Y. Sakai, K. Nagata, Y. Ito, T. Hayase, LES–Lagrangian particle method for turbulent reactive flows based on the approximate deconvolution model and mixing model, J. Comput. Phys. 294 (2015) 127–148.

[26] T. Watanabe, K. Nagata, Mixing model with multi-particle interactions for Lagrangian simulations of turbulent mixing, Phys. Fluids 28 (8) (2016) 085103.

[27] Y. Tai, T. Watanabe, K. Nagata, Modeling of molecular diffusion and

thermal conduction with multi-particle interaction in compressible turbulence, Phys. Fluids 30 (3) (2018) 035108.

[28] C. D. Pierce, P. Moin, A dynamic model for subgrid-scale variance and dissipation rate of a conserved scalar, Phys. Fluids 10 (1998) 3041.

[29] A. W. Cook, W. K. Bushe, A subgrid-scale model for the scalar dissipation rate in nonpremixed combustion, Phys. Fluids 11 (1999) 746.

[30] C. Jiménez, F. Ducros, B. Cuenot, B. Bédat, Subgrid scale variance and dissipation of a scalar field in large eddy simulations, Phys. Fluids 13 (6) (2001) 1748–1754.

[31] T. Watanabe, K. Nagata, Gradients estimation from random points with volumetric tensor in turbulence, J. Comput. Phys. 350 (2017) 518–529.

[32] P. Robert, A. Roux, C. C. Harvey, M. W. Dunlop, P. W. Daly, K. H. Glassmeier, Tetrahedron geometric factors, Analysis Methods for Multi-Spacecraft Data (1998) 323–348.

[33] C. C. Harvey, Spatial gradients and the volumetric tensor, Analysis Methods for Multi-Spacecraft Data (1998) 307–322.

[34] T. Watanabe, C. B. da Silva, K. Nagata, Y. Sakai, Geometrical aspects of turbulent/non-turbulent interfaces with and without mean shear, Phys. Fluids 29 (8) (2017) 085105.

[35] S. B. Pope, Turbulent Flows, Cambridge Univ. Pr., 2000.

[36] T. Watanabe, Y. Sakai, K. Nagata, Y. Ito, Large eddy simulation study of turbulent kinetic energy and scalar variance budgets and

turbulent/non-turbulent interface in planar jets, Fluid Dyn. Res. 48 (2) (2016) 021407.

[37] G. Wei, I. Vinkovic, L. Shao, S. Simoëns, Scalar dispersion by a large-eddy simulation and a Lagrangian stochastic subgrid model, Phys. Fluids 18 (9) (2006) 095101.

[38] G. K. Batchelor, Small-scale variation of convected quantities like temperature in turbulent fluid Part 1. General discussion and the case of small conductivity, J. Fluid Mech. 5 (1959) 113–133.

[39] G. K. Batchelor, I. D. Howells, A. A. Townsend, Small-scale variation of convected quantities like temperature in turbulent fluid Part 2. The case of large conductivity, J. Fluid Mech. 5 (1) (1959) 134–139.

[40] C. B. da Silva, J. C. F. Pereira, Invariants of the velocity-gradient, rate-of-strain, and rate-of-rotation tensors across the turbulent/nonturbulent interface in jets, Phys. Fluids 20 (5) (2008) 055101.

[41] M. van Reeuwijk, M. Holzner, The turbulence boundary of a temporal jet, J. Fluid Mech. 739 (2014) 254–275.

[42] T. Watanabe, C. B. da Silva, Y. Sakai, K. Nagata, T. Hayase, Lagrangian properties of the entrainment across turbulent/non-turbulent interface layers, Phys. Fluids 28 (3) (2016) 031701.

[43] F. Hunger, M. Gauding, C. Hasse, On the impact of the turbulent/non-turbulent interface on differential diffusion in a turbulent jet flow, J. Fluid Mech. 802.

[44] M. M. Rogers, R. D. Moser, Direct simulation of a self-similar turbulent mixing layer, Phys. Fluids 6 (2) (1994) 903–923.

[45] C. Pantano, S. Sarkar, A study of compressibility effects in the high-speed turbulent shear layer using direct simulation, J. Fluid Mech. 451 (2002) 329–371.

[46] M. Gampert, J. Boschung, F. Hennig, M. Gauding, N. Peters, The vorticity versus the scalar criterion for the detection of the turbulent/non-turbulent interface, J. Fluid Mech. 750 (2014) 578–596.

[47] R. D. Moser, M. M. Rogers, D. W. Ewing, Self-similarity of time-evolving plane wakes, J. Fluid Mech. 367 (1998) 255–289.

[48] J. A. Redford, I. P. Castro, G. N. Coleman, On the universality of turbulent axisymmetric wakes, J. Fluid Mech. 710 (2012) 419–452.

[49] M. P. Martín, Direct numerical simulation of hypersonic turbulent boundary layers. Part 1. Initialization and comparison with experiments, J. Fluid Mech. 570 (2007) 347–364.

[50] M. Kozul, D. Chung, J. P. Monty, Direct numerical simulation of the incompressible temporally developing turbulent boundary layer, J. Fluid Mech. 796 (2016) 437–472.

[51] T. Watanabe, X. Zhang, K. Nagata, Turbulent/non-turbulent interfaces detected in DNS of incompressible turbulent boundary layers, Phys. Fluids 30 (3) (2018) 035102.

[52] X. Zhang, T. Watanabe, K. Nagata, Turbulent/non-turbulent interfaces in high resolution direct numerical simulation of temporally-evolving compressible turbulent boundary layers, Phys. Rev. Fluids (2018) Accepted for publication.

[53] A. Kempf, M. Klein, J. Janicka, Efficient generation of initial-and inflow-conditions for transient turbulent flows in arbitrary geometries, Flow, Turbul. Combust. 74 (1) (2005) 67–84.

[54] O. Terashima, Y. Sakai, K. Nagata, Simultaneous measurement of velocity and pressure in a plane jet, Exp. Fluids 53 (4) (2012) 1149–1164.

[55] E. Gutmark, I. Wygnanski, The planar turbulent jet, J. Fluid Mech. 73 (1976) 465–495.

[56] B. R. Ramaprian, M. S. Chandrasekhara, LDA measurements in plane turbulent jets, Trans. ASME: J. Fluids Engng. 107 (2) (1985) 264–271.

[57] M. Klein, A. Sadiki, J. Janicka, Investigation of the influence of the Reynolds number on a plane jet using direct numerical simulation, Int. J. Heat Fluid Flow 24 (6) (2003) 785–794.

[58] T. Watanabe, J. J. Riley, K. Nagata, R. Onishi, K. Matsuda, A localized turbulent mixing layer in a uniformly stratified environment, J. Fluid Mech. 849 (2018) 245–276.

[59] Y. Morinishi, T. S. Lund, O. V. Vasilyev, P. Moin, Fully conservative higher order finite difference schemes for incompressible flow, J. Comput. Phys. 143 (1) (1998) 90–124.

[60] I. Namer, M. V. Ötügen, Velocity measurements in a plane turbulent air jet at moderate Reynolds numbers, Exp. Fluids 6 (6) (1988) 387–399.

[61] L. K. Su, N. T. Clemens, The structure of fine-scale scalar mixing in gas-phase planar turbulent jets, J. Fluid Mech. 488 (2003) 1–29.

[62] P. S. Kothnur, N. T. Clemens, Effects of unsteady strain rate on scalar dissipation structures in turbulent planar jets, Phys. Fluids 17 (12) (2005) 125104.

[63] T. Watanabe, J. J. Riley, K. Nagata, Effects of stable stratification on turbulent/nonturbulent interfaces in turbulent mixing layers, Phys. Rev. Fluids 1 (4) (2016) 044301.

[64] T. S. Silva, C. B. da Silva, The behaviour of the scalar gradient across the turbulent/non-turbulent interface in jets, Phys. Fluids 29 (8) (2017) 085106.

[65] C. A. Kennedy, M. H. Carpenter, Several new numerical methods for compressible shear-layer simulations, Appl. Numer. Math. 14 (4) (1994) 397–433.

[66] M. Gampert, V. Narayanaswamy, P. Schaefer, N. Peters, Conditional statistics of the turbulent/non-turbulent interface in a jet flow, J. Fluid Mech. 731 (2013) 615–638.

[67] T. Watanabe, Y. Sakai, K. Nagata, Y. Ito, T. Hayase, Turbulent mixing of passive scalar near turbulent and non-turbulent interface in mixing layers, Phys. Fluids 27 (8) (2015) 085109.

[68] T. S. Silva, M. Zecchetto, C. B. da Silva, The scaling of the turbulent/non-turbulent interface at high Reynolds numbers, J. Fluid Mech. 843 (2018) 156–179.